Upper tropospheric ice sensitivity to sulfate geoengineering

Daniele Visioni[1,2], Giovanni Pitari[1], and Glauco di Genova[2]

[1]Department of Physical and Chemical Sciences, Universitá dell'Aquila, 67100 L'Aquila, Italy
[2]CETEMPS, Universitá dell'Aquila, 67100 L'Aquila, Italy

Abstract. Aside from the direct surface cooling sulfate geoengineering (SG) would produce, the investigation on possible side-effects of this method is still ongoing, as for instance on upper tropospheric cirrus cloudiness. Goal of the present study is to better understand the SG thermo-dynamical effects on the homogeneous freezing ice formation process. This is done by comparing SG model simulations against a RCP4.5 reference case: in one case the aerosol-driven surface cooling is included and coupled to the stratospheric warming resulting from aerosol absorption of longwave radiation. In a second SG perturbed case, surface temperatures are kept unchanged with respect to the reference RCP4.5 case. Surface cooling and lower stratospheric warming, together, tend to stabilize the atmosphere, thus decreasing turbulence and water vapor updraft velocities (-10% in our modeling study). The net effect is an induced cirrus thinning, which may then produce a significant indirect negative radiative forcing (RF). This would go in the same direction as the direct effect of solar radiation scattering by the aerosols, thus influencing the amount of sulfur needed to counteract the positive RF due to greenhouse gases. In our study, given a 8 Tg-SO_2 equatorial injection in the lower stratosphere, an all-sky net tropopause RF of -2.13 W/m^2 is calculated, of which -0.96 W/m^2 (45%) from the indirect effect on cirrus thinning (7.5% reduction in ice optical depth). When the surface cooling is ignored, the ice optical depth reduction is lowered to 5%, with an all-sky net tropopause RF of -1.45 W/m^2, of which -0.21 W/m^2 (14%) from cirrus thinning. Relatively to the clear-sky net tropopause RF due to SG aerosols (-2.06 W/m^2), the cumulative effect of background clouds and cirrus thinning accounts for -0.07 W/m^2, due to close compensation of large positive shortwave (+1.85 W/m^2) and negative longwave adjustments (-1.92 W/m^2). When the surface cooling is ignored, the net cloud adjustment becomes +0.71 W/m^2, with the shortwave contribution (+1.97 W/m^2) significantly larger in magnitude than the longwave one (-1.26 W/m^2). This highlights the importance of including all dynamical feedbacks of SG aerosols.

1   Introduction

Sulfate geoengineering (SG) is one of the methods that have been proposed in the scientific community (Budyko (1974); Crutzen (2006); Niemeier and Tilmes (2017)) in order to cool our planet for a limited amount of time, in response to the warming caused by increasing greenhouse gases of anthropogenic origin. SG proposes the injection of SO_2 in the tropical lower stratosphere in order to produce an optically active cloud of H_2SO_4-H_2O supercooled liquid aerosols that would reflect part of the incoming solar radiation back to space. These aerosols, however, would at the same time warm the lower stratosphere by a few degrees. The idea stems from the cooling effect of past explosive volcanic eruption in the tropical region (the last being Pinatubo in 1991). These major eruptions injected large amounts of SO_2 in the lower stratosphere and increased the planetary

albedo. The resulting cooling effect has been clearly observed (Robock (2000)), although the magnitude of this cooling is still being discussed (Canty et al. (2013)).

In the case of past volcanic eruptions, both direct and indirect effects of episodic large injection of sulfur in the stratosphere have been observed and documented, this is obviously not possible for planned sustained sulfur injection in SG experiments.

5 Because of this, the scientific community mainly relies on simulations using climate models and comparison of results among them, as for instance under the GeoMIP project (Kravitz et al. (2011); Kravitz et al. (2013)). Different injection scenarios have been proposed and adopted in modelling experiments, the most used being the one with a constant sulfur injection rate at the equator for a certain number of years, in order to understand the climate response to such an atmospheric perturbation. Simulations have also been performed to identify the magnitude and location of the sulfur injection, in order to obtain the highest

10 ratio between radiative forcing (RF) and injection magnitude (Niemeier and Schmidt (2017); Tilmes et al. (2017); Kleinschmitt et al. (2017)).

Amongst various side effects of SG, those with non-negligible impact on RF were analysed and summarized in Visioni et al. (2017a). These are related to an enhancement of stratospheric ozone destruction (Tilmes et al. (2008); Pitari et al. (2014); Xia et al. (2017)), an increase in the concentration and lifetime of methane (Visioni et al. (2017b)), an increase of stratospheric

15 water vapor due to a TTL warming (Pitari et al. (2014)) and most importantly to a change in the probability of formation of cirrus ice particles in the upper troposphere (UT) (Kuebbeler et al. (2012)). Regarding this latter effect, some studies have appeared in recent literature that propose ways in which SG could affect UT cirrus ice number density and optical depth. We will discuss them below and try to expand some aspects further in the present work.

20 Fig. 1 summarizes in a schematic way those dynamical and radiative processes related to UT ice formation that we analyze in detail ahead in this paper. In an unperturbed atmosphere, formation of UT ice particles may take place either by homogeneous or heterogeneous freezing (Karcher and Lohmann (2002); Hendricks et al. (2011)), with the former process normally dominating over the latter. Homogeneous freezing takes place when the ice supersaturation ratio is relatively high (typically above ∼1.5), local temperatures are below the threshold for atmospheric ice particle formation (∼238 K) and supercooled

25 solution droplets are present, namely sulfate aerosols or sulfate coated aerosols. Supersaturation conditions is maintained by intense vertical motions bringing water vapor from the lower to the upper troposphere.

Ice crystals formed this way both reflect part of the incoming solar radiation (negative RF) and trap part of the outgoing planetary radiation contributing to the greenhouse effect (positive RF). The sign of the combined effects could not easily be

30 determined in a variety of atmospheric conditions. Normally, however, it has been shown that the net UT ice contribution to RF is positive (Chen et al. (2000); Fusina et al. (2007); Gasparini et al. (2017)). This is, anyway, a rather delicate balance and strongly depending on humidity and cloud cover (Sanderson et al. (2008); Mitchell et al. (2008)), so that a robust atmospheric perturbation, such as the one SG could produce, may significantly affect it.
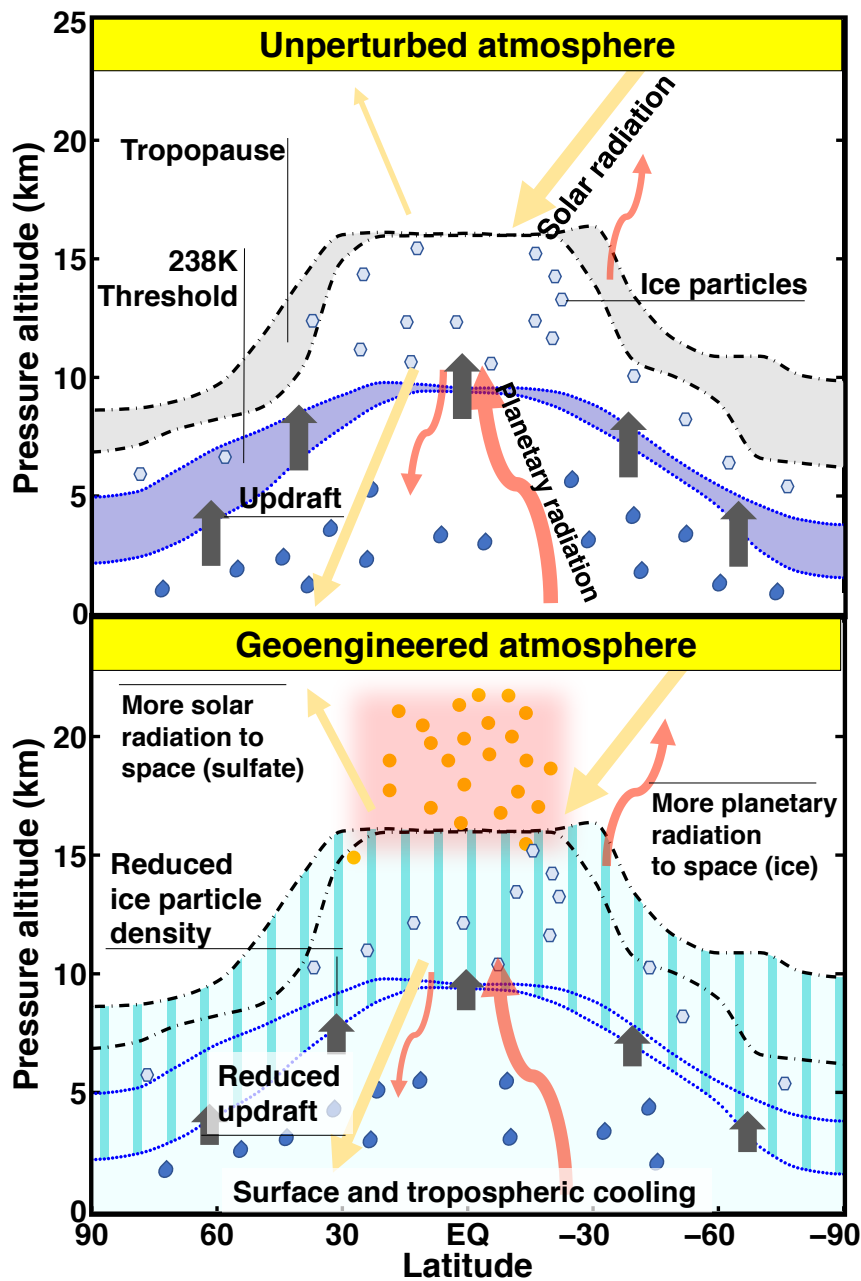
Figure 1. Cartoon of the sulfate geoengineering impact on cirrus ice particles, formed through homogeneous freezing, and schematic representation of ice induced changes in radiative fluxes.

The perturbation to UT ice could be twofold. On one hand, Cirisan et al. (2013) studied how the H_2SO_4-H_2O droplets resulting from the sulfur injection would interact with cirrus clouds, both microphysically and radiatively. Even if an increase in

ice nuclei (IN) in the upper troposphere were found, the positive RF associated to this effect would be negligible, as the authors themselves state in their study. Kuebbeler et al. (2012), on the other hand, analyzed the effects produced by dynamical changes due to modification of the tropospheric thermal gradient produced by stratospheric geoengineering aerosols. In particular, the lower stratosphere (LS) warming, caused by increasing heating rates in the optically thick sulfate cloud, tends to decrease

5 the tropospheric lapse rate. A subsequent decrease in the available turbulent kinetic energy (TKE) would follow and translate in slowing down updraft of water vapor to the UT, thus reducing the probability for sufficiently high supersaturation values capable to produce ice crystals formation via homogeneous freezing. Their study found a resulting large net RF reduction in magnitude with respect to clear sky conditions, where only the direct aerosol forcing is considered (-0.93 W/m^2 against -1.53 W/m^2). They conclude that this forcing reduction results not only from the mere (passive) presence of background clouds

10 which affect the atmospheric radiative transfer, but also from the cirrus cloud thinning produced by SG aerosols. This may obviously have clear implication regarding the potential of SG to counterbalance global warming.

The aforementioned study, however, lacked an important part of the possible dynamical feedback of SG, that is changes in sea surface temperatures (SSTs) that would result from the decreased incoming solar radiation. Goal of the present study

15 is to study the SG impact on cirrus ice particles formed via homogeneous freezing, by include the two main radiative effects of stratospheric sulfate, i.e., local warming and surface cooling: this is made using the composition-climate coupled model developed at the University of L'Aquila (ULAQ-CCM). We performed a SG simulation with a 8 Tg-SO$_2$/yr injection, using surface temperatures calculated in the atmosphere-ocean coupled model CCSM-CAM4 operated with the same sulfur injection (thus resulting in a general surface cooling, with respect to atmospheric unperturbed conditions). This perturbed experiment

20 (named G4, according to the convention of Kravitz et al. (2011), regardless from the time constant magnitude of the injection), is compared against a baseline simulation without SG and using a background anthropogenic emission scenario corresponding to the Representative Concentration Pathway 4.5 (RCP4.5) (Taylor et al. (2012)) (named Base case in our study). In order to properly compare our results with the ones of Kuebbeler et al. (2012), a third simulation was performed with the same geo-engineering sulfur injection of G4, but with surface temperatures fixed at the Base case values (named G4K).

The effects of SG surface temperature changes on the lower stratospheric dynamics were already discussed in Visioni et al. (2017b); this time we focus on their impact in the upper troposphere. A flow-chart summary of the dynamical-radiative effects of SG on the UT is presented in Fig. 2, in a way that the SG-driven surface cooling effects are clearly highlighted. In particular, while both SG simulations (G4 and G4K) have the lower stratospheric warming in common, the surface (and consequently tro-

30 pospheric) cooling is present only when surface temperatures are allowed to respond to the decreased incoming solar radiation (i.e., only in G4). This produces partially compensating effects on cirrus ice formation: a decrease in probability due to less water vapor updraft and an increase in probability due to colder temperatures in the UT. Colder temperatures, in fact, allow for a number density increase of ice particles (and their reduction in size), due to slower depositional growth and higher nucleation rate (Visioni et al. (2017a)). The predominant effect, as discussed ahead in Section 3, is the one related to changes in vertical

35 motion, which produce an overall decrease in ice optical depth so that, in turn, more planetary radiation is allowed to escape to
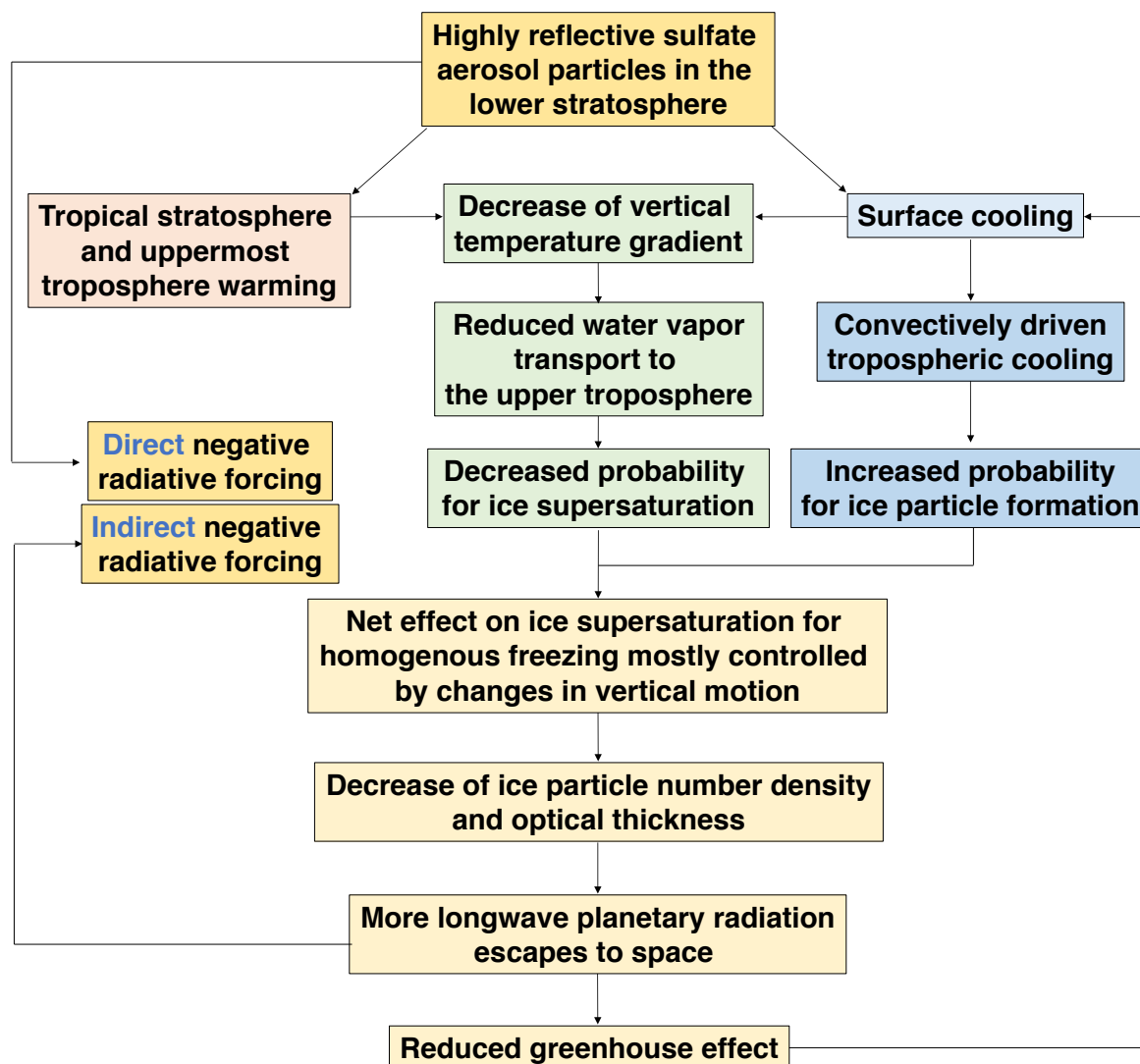
Figure 2. Schematic summary of the sulfate geoengineering impact on dynamical processes driving changes of upper tropospheric ice particle formation through homogeneous freezing.

space with an indirect negative RF (i.e., reduced greenhouse effect).

Unlike other side effects of sulfur injection in the stratosphere, a comparison between the effects of a volcanic eruption and SG on cirrus ice is hard to draw. This is mainly due to the fact that in a volcanic eruption episode (contrary to SG), a

5   large amount of solid ash particles is injected in the lower stratosphere together with SO_2. Part of these dust particles, after settling down below the tropopause, may contribute to increase the number density of IN available for heterogeneous freezing

in the UT. This could help explain some observed increase in UT ice particles after the Pinatubo eruption (Sassen et al. (2008)).

Understanding the RF contribution of the UT ice perturbation in a SG scenario is particularly crucial if the scientific community wants to design experiments whose goal is to meet a given climate target, as proposed in Kravitz et al. (2017) and
5 MacMartin et al. (2017).

This paper is structured in 3 subsequent sections plus the conclusions: in Section 2 we describe the ULAQ-CCM model and the set-up of the numerical experiments, discussing the dynamical drivers that may explain the ice perturbations described later on. Furthermore, in Section 2 we try to evaluate the model skill in simulating the formation of cirrus ice clouds, using re-analysis and satellite data. In Section 3 we discuss the model calculated changes in cirrus cloudiness (mass fraction, optical depth,
10 number concentration, particle size) produced by SG and finally we show how these perturbations translate into tropopause radiative forcing terms.

2   ULAQ-CCM and setup of numerical experiments

The use of a composition-climate coupled model, as the ULAQ-CCM model, offers multiple advantages in this type of study:
15 (a) on-line inclusion of interaction between aerosol and ice particles microphysics with chemistry, radiation, climate, dynamics and transport; (b) stratosphere-troposphere explicit interactions for the large-scale transport of gas and aerosol species (the model adopted high vertical resolution is important across the tropopause region); (c) sufficiently detailed chemistry both in the stratosphere and troposphere, with a robust design for heterogeneous chemical reactions on sulfuric acid aerosols, polar stratospheric cloud particles, upper tropospheric ice and liquid water cloud particles. This allows to account for atmospheric
20 circulation changes produced by sulfate geoengineering. The ULAQ-CCM has many times proven to be capable of producing sound physical and chemical responses to both sulfate geoengineering (Pitari et al. (2014); Visioni et al. (2017b)) and for large explosive volcanic eruptions (Pitari (1993); Pitari et al. (2016b); Pitari et al. (2016a)).

In addition to a reference historical model experiment (1960-2015), we performed three sets of SG simulations: a baseline
25 (Base) unperturbed case and two geoengineering experiments (G4 and G4K), both run with an injection of 8 Tg-SO_2/yr in the equatorial stratosphere between 18 and 25 km of altitude, as described in Kravitz et al. (2011) for the GeoMIP G4 experiment with sustained fixed injection of sulfur dioxide (5 Tg-SO_2/yr in that case). These numerical experiments were all run between years 2020-2069, with analyses focusing on the 2030-2039 decade; all take place under the same RCP4.5 reference scenario for well mixed greenhouse gases. The ULAQ-CCM is not an atmosphere-ocean coupled model and uses a nudging technique for
30 surface temperatures, taking them from the CCSM-CAM4 model, which was run under the same RCP4.5 and G4 conditions (8 Tg-SO_2/yr fixed injection in the equatorial lower stratosphere). In this way our main experiment G4 may account for the oceanic surface temperature response to SG (Fig. 3-4), even if only at a first order approximation since, as we will show, the

cooling produced when also considering ice clouds modifications might be different.

A strong inter-hemispheric asymmetry in surface temperature changes produced by SG with 8 Tg-SO$_2$/yr injection is evident in both Fig. 3-4, with a negative anomaly in the Arctic region larger than 1 K with respect to south polar latitudes. The

5 SG cooling impact on Arctic sea ice is such that larger negative surface temperature anomalies are favored in the Northern Hemisphere high latitudes for several months during the year, from fall to spring months (see Fig. 3a, Fig. 3b, Fig. 3d), thus increasing atmospheric stabilization with respect to the Southern Hemisphere. It should be noted, however, that the dynamical effects of this enhanced atmospheric stability in SG conditions (decreasing wave activity and turbulence) may be partially counterbalanced by the increased longitudinal variability of the induced cooling, mostly connected with positive surface tem-

10 perature anomalies in the subpolar North Atlantic. These positive temperature anomalies in the North Atlantic sub-Arctic are a direct consequence of the increasing amount of polar sea ice in SG conditions, with southward transport of colder and saltier ocean waters in the sub-Arctic, with respect to RCP4.5 Base conditions (Tilmes et al. (2009)). In this way, the North Atlantic subpolar downwelling of these cold surface waters to the deep ocean is favored with respect to Base conditions, thus producing positive anomalies in sea surface temperatures.

The SG induced warming on the Antarctic continent during wintertime (Fig. 3c), on the other hand, is a direct consequence of the geoengineering aerosol positive radiative forcing in the planetary longwave, which represent the net forcing at these high latitudes in the absence of sunlight. This radiative feature will be further discussed in Section 3. All these high-latitude positive temperature anomalies directly reflect in a large variability of the zonally averaged surface temperature changes presented in

20 Fig. 4.

Together with the G4 simulation, a sensitivity case (G4K) was run, with surface temperatures fixed at the RCP4.5 Base values. Here the experimental approach is similar to that of Kuebbeler et al. (2012) who ran a G4 simulation with 5 Tg-SO$_2$/yr injection and prescribed sea surface temperatures and sea ice from the RCP4.5 Base case. This is done in order to highlight not only the role of tropospheric temperature perturbations in cirrus ice formation (given a certain vertical velocity change), but

25 mostly to calculate the updraft sensitivity to different conditions of tropospheric stabilization introduced by the stratospheric sulfate aerosol injection. Fig. 5 shows the differences in temperature and updraft in G4 and G4K with respect to the Base case. In G4 we observe a tropospheric cooling of $\simeq$1-2 K in the ice formation region throughout all latitudes, while the warming due to sulfate aerosol absorption of shortwave and longwave radiation is confined above the tropopause (Fig. 5a). When surface temperatures are kept fixed at the RCP4.5 baseline values with the SG perturbation (G4K case), the upper troposphere

30 and lower stratosphere temperature anomalies look very different (Fig. 5b). The tropospheric cooling is absent and the stratospheric warming produced by longwave and near-infrared solar radiation absorption is more uniformly spread across the lower stratosphere, with some penetration also in the UT ($\simeq$0-1 K). The latter is due to sulfate aerosol cross-tropopause large-scale transport (at mid-latitudes) and gravitational sedimentation (mostly relevant in the tropical region).

Updraft responsible for upper tropospheric ice particle formation results from the sum of a rather small large-scale vertical

35 velocity contribution (on the order of 1-2 cm/s) and a dominant part due to motions associated to synoptic scale disturbances
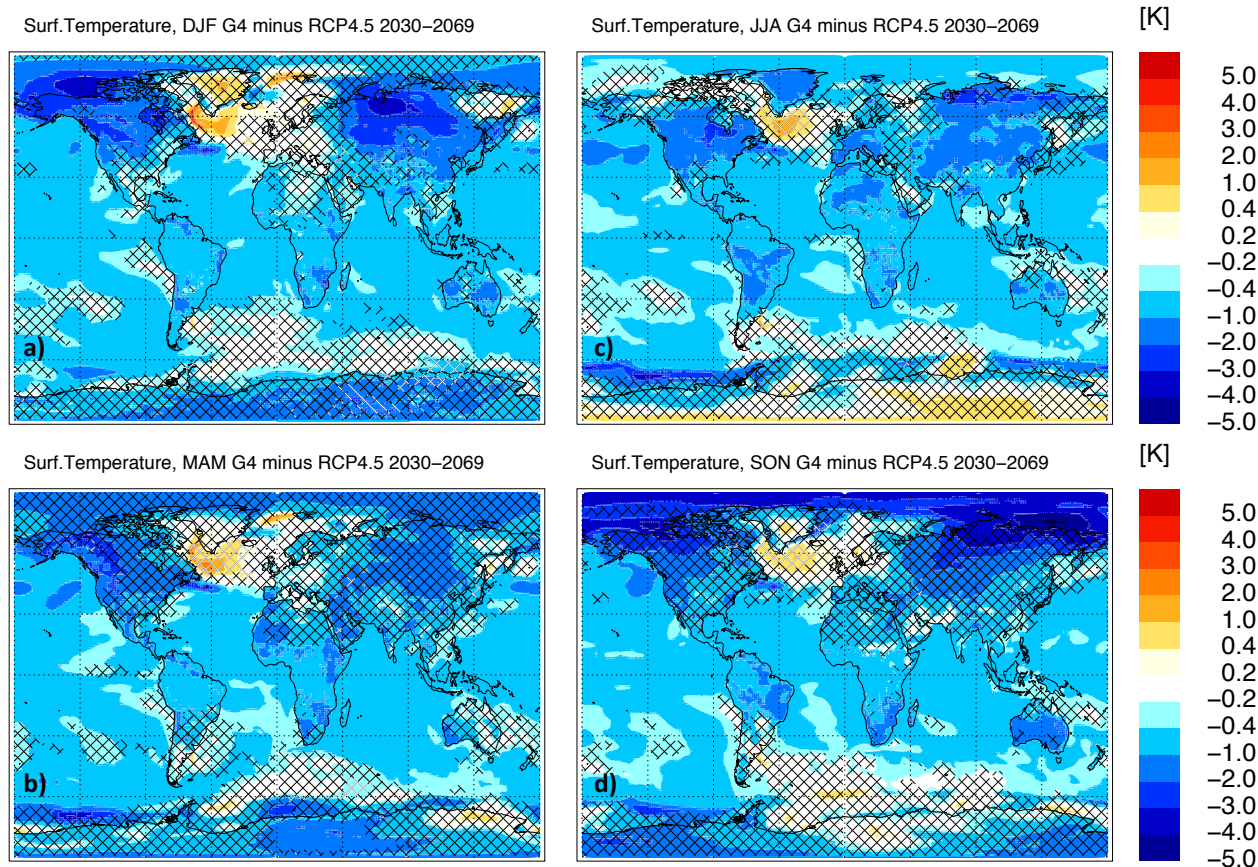
Figure 3. Seasonally averaged surface temperature anomalies G4-RCP4.5 (K), from the atmosphere-ocean coupled model CCSM-CAM4 (time average 2030-2069). Shaded areas are not statistically significant within $\pm 1\sigma$. Panels (a-d) refer to: December-January-February (a); March-April-May (b); June-July-August (c); September-October-November (d).

and gravity waves (on the order of 10-20 cm/s); the latter is calculated as a function of the TKE (Lohmann and Karcher (2002)). The vertical velocity is reduced in G4 with respect to the Base case by $\simeq$1-2 cm/s in the whole UT (Fig. 5c) (on the order of -10%, as visible in Fig. 6), due to the atmospheric stabilization caused by the reduction in the temperature gradient.

5   The SG induced reduction of updraft velocities is significantly smaller in the G4K case ($\simeq$0.5 cm/s, on the order of -3% the baseline values), as clearly visible in Fig. 5d. This will represent the major change in our approach for studying the UT ice sensitivity to SG, with respect to the one adopted in Kuebbeler et al. (2012). According to our calculations, when taking into account both the main radiative effects of geoengineering stratospheric aerosols (i.e., lower stratospheric heating on one hand, surface and tropospheric cooling on the other hand) the resulting impact on tropospheric turbulence and updraft is significantly
10   enhanced with respect to the case in which only the stratospheric warming is considered. A noticeable difference in the G4K
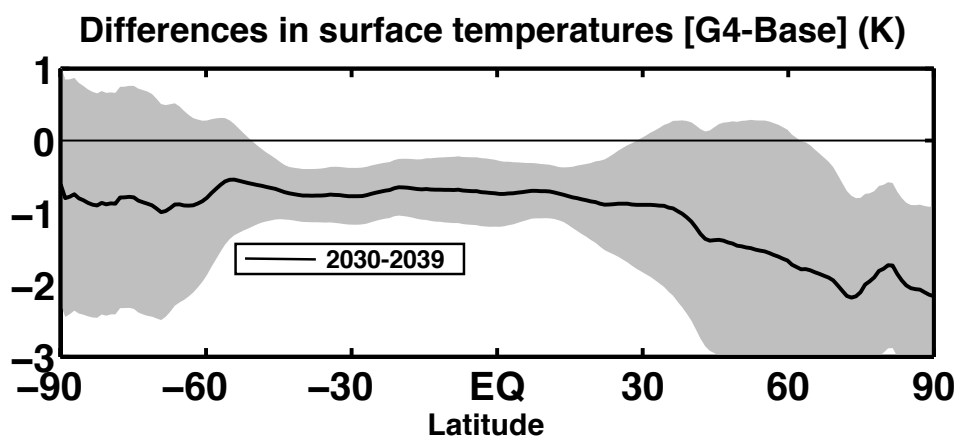
Figure 4. Annually and zonally averaged surface temperature anomalies G4-RCP4.5 (K), from the atmosphere-ocean coupled model CCSM-CAM4 (time average 2030-39). The shaded area represents $\pm 1\sigma$ of the zonally averaged temperature anomalies over the 10 year period.

w-anomalies with respect to the G4 ones is at low altitudes over the polar regions, where the G4K negative values are larger than in G4. This may be largely explained by the increasing longitudinal variability of surface temperatures in the G4 case, mainly in the sub-Arctic region (see previous discussion relative to Fig. 3).

5   Tropical and extratropical average profiles of the updraft velocity are shown in Fig. 6, for both Base and G4 conditions. The G4K curve (not shown) is intermediate between the previous two. The pronounced variability of the vertical velocity is expected as a consequence of time, latitude and longitude fluctuations of TKE. This will produce a significant dispersion of the ice particle size distribution (see ahead in Section 3).

10   A compact summary of model features in these numerical experiments is presented in Table 1; relevant aerosol and ice quantities calculated in the ULAQ-CCM are summarized in Table 2 in comparison with available satellite observations. The first two rows in Table 2 compare the ULAQ-CCM results for stratospheric sulfate optical depth (OD) and tropical effective radius (r_{eff}) against SAGE-II and AVHRR satellite observations (Thomason et al. (1997); Long and Stowe (1994)), under post-Pinatubo conditions (Pitari et al. (2016a)). This is done to highlight the realistic representation of gas-particle conversion
15   and aerosol microphysics processes in the model, along with aerosol large scale transport in the lower stratosphere in case of a major tropical volcanic eruption, which may be used as a proxy for SG with an equatorial SO_2 injection. A comparison of aerosol effective radii under volcanic and background conditions (see rows 2 and 3 in Table 2), clearly shows the effects of sulfuric acid condensation on the size extension of the aerosol accumulation mode and how this is represented in the model. The bottom 5 rows in Table 2 compare global budget calculations for upper tropospheric ice particles with values obtained from
20   MERRA reanalyses (ice mass fraction) and MODIS retrieval (ice effective radius). Simultaneous use of these two products
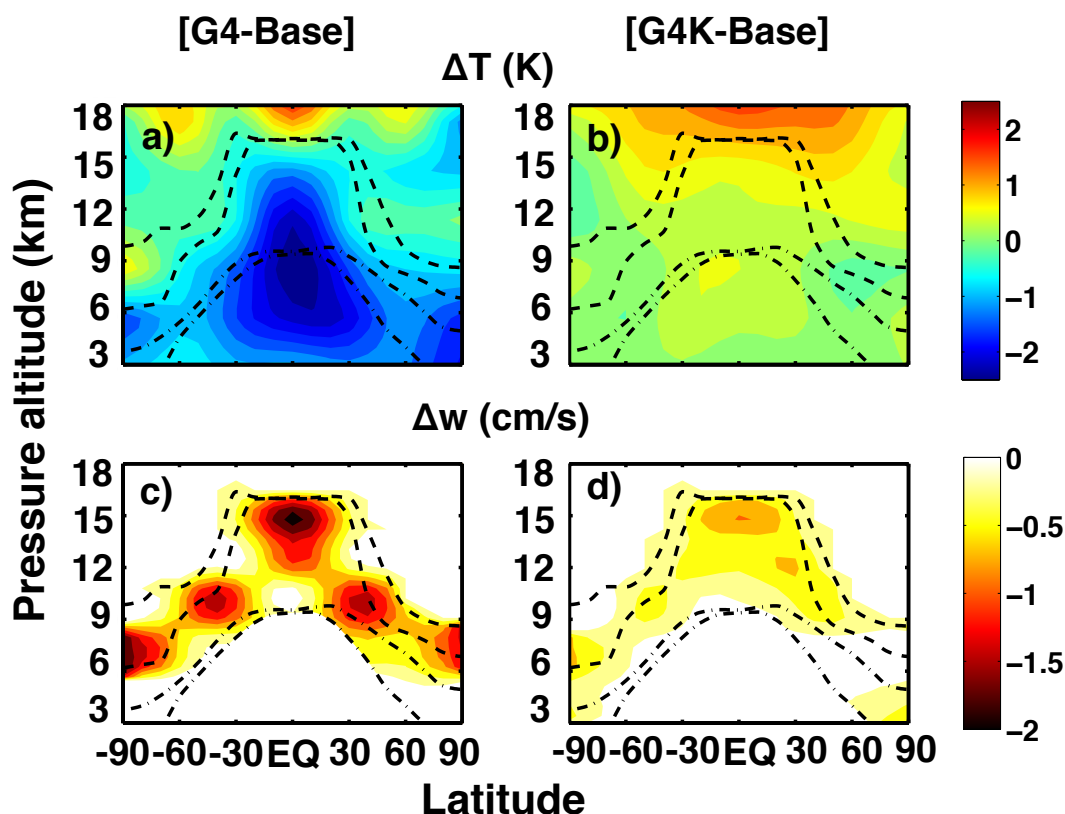
Figure 5. Zonally and time averaged changes of temperature (panels a,b) and vertical velocity (panels c,d) in experiments G4 (panels a,c) and G4K (panels b,d) with respect to the Base case (years 2030-39). The dashed lines show the mean tropopause height (with seasonal variability). The dash-dotted lines show the mean height (with seasonal variability) at which the temperature reaches 238 K, thus enabling homogeneous freezing.

allows an indirect calculation of the ice optical depth (row 7 of Table 2), as discussed ahead in Section 2.2. The ULAQ-CCM OD underestimation is mostly related to the ice mass fraction lower values in the largest portion of the upper troposphere (see row 5 of Table 2) and may be in part explained with the inclusion of a relatively narrow interval for updraft velocities (w<30 cm/s), as well as with the inclusion of a single pathway for ice particle formation in the model (i.e., via homogeneous freezing).

5   The ULAQ-CCM has been widely described in recent literature, along with in-depth process-evaluation. For the sake of completeness, however, we discuss in the following two sub-headings some of the model features, in particular those relevant for stratospheric sulfate aerosols and upper tropospheric cirrus ice particle formation.
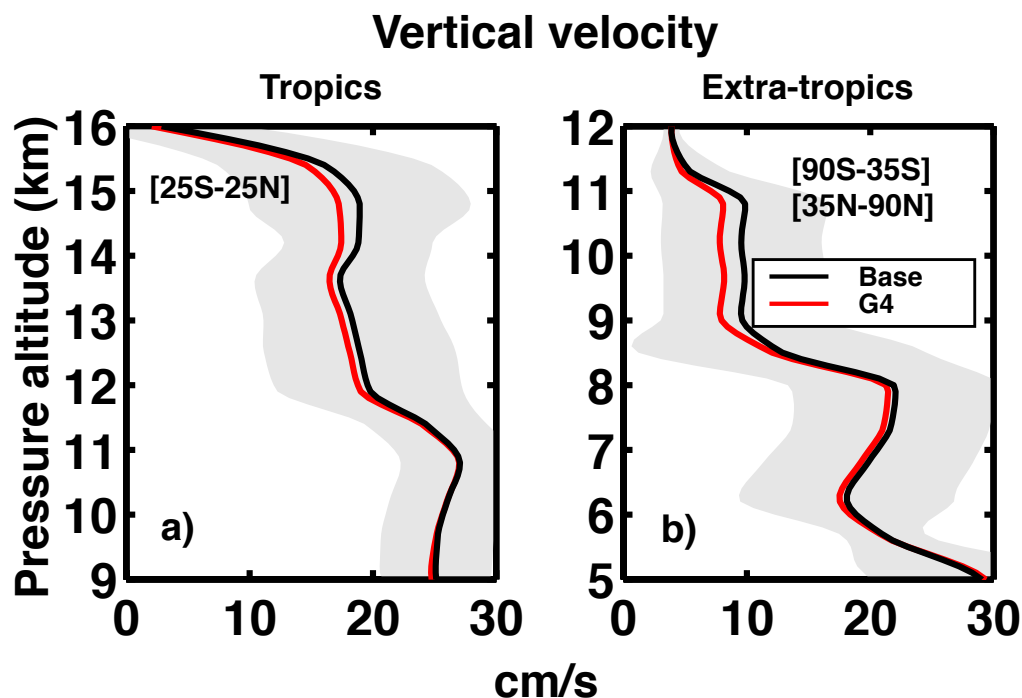
Figure 6. Average upper tropospheric profiles of the vertical velocity (cm/s) in G4 and Base experiments (years 2030-39). Panels (a) and (b) are for the tropics and extratropics, respectively (see legends). The vertical velocity w is obtained as the sum of the large scale value and the one calculated as a function of turbulent kinetic energy (see Lohmann and Karcher (2002)), which essentially accounts for synoptic scale and gravity wave motions. Shaded areas of the same color represent $\pm 1\sigma$ for the ensemble over the 10 year period 2030-39.

Table 1. Summary of ULAQ-CCM features and numerical experiments for the present study.

Years of simulation	1960-2015	2020-2069
Type of simulation	Reference	Base (RCP4.5) + G4 + G4K
Ensemble size	2	1 +2 + 2
Horizontal and vertical resolution	$5° \times 6°$, L126 log-pressure top: 0.04 hPa	
Chemistry	On-line (strat & trop)	
Dynamics	Calculated[1]	Calculated[2]
QBO	Nudged (from equatorial wind obs.)	Nudged (iteration of observed cycles of eqt. winds)
Altitude of equatorual injection of SO_2 in G4 (8 Tg-SO_2/yr)	-	18 -25 km (Gaussian Distribution)

[1] Sea surface temperatures from observations; calculated land temperatures

[2] Surface temperatures from CCSM-CAM4, separately for Base and G4 (Visioni et al. (2017b))

[3] Surface temperatures from CCSM-CAM4, Base values used also for G4K

Table 2. Summary of time-averaged sulfate aerosol and cirrus ice particle related quantities, as calculated in the ULAQ-CCM and compared with available satellite observations. Sulfate aerosols: sectional approach (Pitari et al. (2002); Pitari et al. (2014)). Cirrus ice particles: parameterization for homogenous freezing based on Karcher and Lohmann (2002), but including effects of the aerosol size distribution; a probabilistic approach is adopted for the ice supersaturation ratio. Standard deviations are calculated over the time series of globally averaged monthly mean values.

Stratospheric sulfate optical depth	0.11 ± 0.02 (ULAQ-CCM)
[post-Pinatubo conditions]	0.13 ± 0.02 (SAGE II)
[reference (September 1991 - August 1992)]	0.13 ± 0.02 (AVHRR)
Sulfate r_{eff} (μm) (30-100 hPa, 25S-25N)	
[post-Pinatubo conditions]	0.54 ± 0.06 (ULAQ-CCM
[reference (September 1991 - August 1992)]	0.58 ± 0.06 (SAGE II)
Sulfate r_{eff} (μm) (30-100 hPa, 25S-25N)	
[volcanic unperturbed conditions]	0.19 ± 0.02 (ULAQ-CCM
[reference (1999 - 2000)]	0.22 ± 0.02 (SAGE II)
Ice mass fraction (mg/kg) (150-200 hPa)	3.3 ± 0.3 (ULAQ-CCM)
[reference (2003 - 2012)]	3.5 ± 0.4 (MERRA)
Ice mass fraction (mg/kg) (200-300 hPa)	4.3 ± 0.6 (ULAQ-CCM)
[reference (2003 - 2012)]	5.5 ± 0.8 (MERRA)
Ice mass fraction (mg/kg) (350-400 hPa)	2.5 ± 0.4 (ULAQ-CCM)
[reference (2003 - 2012)]	2.6 ± 0.5 (MERRA)
Upper tropospheric ice r_{eff} (μm)	32.0 ± 3.6 (ULAQ-CCM)
[reference (2003 - 2012)]	33.4 ± 2.1 (MODIS)
Upper tropospheric ice optical depth	0.40 ± 0.03 (ULAQ-CCM)
[reference (2003 - 2012)]	0.62 ± 0.04 (MERRA+MODIS)

2.1 Stratospheric sulfate aerosols

The University of L'Aquila composition-climate coupled model was described in its first version in Pitari et al. (2002); subsequent model versions were documented in modeling intercomparison campaigns (Eyring et al. (2006); Morgenstern et al. (2010); Morgenstern et al. (2017)). Model updates in horizontal and vertical resolution, photolysis cross sections, treatment of Schumann-Runge bands and radiative transfer code were described and tested in Pitari et al. (2014) and Chipperfield et al. (2014). The shortwave radiative module has been documented and tested for tropospheric aerosols in Randles et al. (2013) and also for volcanic stratospheric aerosols in Pitari et al. (2016a). It makes use of a two-stream delta-Eddington approximation and is on-line in the model for both photolysis and solar heating rate calculations. A companion broadband, k-distribution longwave radiative module is used for heating rate and top-of-atmosphere radiative forcing calculations in the planetary infrared

spectrum (Chou (2001)).

A critical atmospheric region in SG studies is the upper troposphere and lower stratosphere (UTLS). An extensive model evaluation based on specific physical and chemical aspects was made in Gettelman et al. (2010) and Hegglin et al. (2010)). Subsequent model improvements in this region were discussed in Pitari et al. (2016b). The treatment of surface temperatures,

5   and their importance for the lower stratospheric dynamics and species transport under a geoengineering scenario, has been discussed in Visioni et al. (2017b). Another very important aspect to be taken into account for large-scale species transport in the lower stratosphere is the role of the quasi-biennial oscillation (QBO) in SG studies. It has been discussed under different points of view in some recent studies (Aquila et al. (2014); Niemeier and Schmidt (2017); Visioni et al., 2017c). A nudging procedure for the QBO is used in the ULAQ-CCM, based on an observed historical data series of equatorial mean zonal winds

10   (Morgenstern et al. (2017)).

In SG experiments G4 and G4K, SO_2 is injected at the equator (0° longitude), throughout the altitude range 18-25 km with a Gaussian distribution centered at 21.5 km. OH oxidation of SO_2 starts the production of supercooled H_2O-H_2SO_4 particles, whose size distribution is calculated in an aerosol microphysics module with sectional approach, starting from gas-particle interaction processes (nucleation, H_2SO_4 condensation and H_2O growth) and then including aerosol particle coagulation. Re-

15   moval processes from are included via gravitational settling across the tropopause and evaporation in the upper stratosphere (Visioni et al. (2017c)).

In the troposphere, the ULAQ-CCM includes sulfate production from DMS and SO_2 emissions, with gas phase and aqueous/ice SO_2 oxidation (by OH and H_2O_2, O_3, respectively) to produce SO_4 (Feichter et al. (1996); Clegg and Abbatt (2001)). The tropospheric and stratospheric SOx budget in the ULAQ-CCM (for unperturbed background conditions) was recently dis-

20   cussed in Pitari et al. (2016c), with focus on the role of non-explosive volcanic sulfur emissions, and in Visioni et al. (2017c) in connection with SG.

Aerosol extinction, optical thickness, single scattering albedo and surface area density are calculated on-line at all model gridpoints every hour. This allows interactive calculation of up/down diffuse radiation and absorption of solar near-infrared and planetary radiation by SG aerosols, with explicit full coupling of aerosol, chemistry and radiation modules in the ULAQ-CCM.

25   This justifies the 'composition-climate' name for this coupled model, which is more general than the usual 'chemistry-climate' model name.

The ULAQ-CCM ability in producing the correct confinement of sulfate aerosols in the tropical stratosphere has already been documented in literature, with comparison against SAGE II data following the Pinatubo eruption or looking at SG conditions (see Pitari et al. (2014); Pitari et al. (2016a); Visioni et al. (2017b)). Figure 7a shows the average tropical vertical profiles of

30   SO_4 mixing ratio, for both Base and SG experiments (with 8 Tg-SO_2 injection). Changes in zonally averaged net heating rates, temperatures and zonal winds are also shown in Fig. 7, panels (b), (c) and (d), respectively. They help to understand how SG sulfate changes act as drivers for dynamical changes in the UT, with significant effects on ice particle formation.

In Fig. 7a it is interesting to note a somewhat smaller tropical aerosol confinement in the G4K case. This is consistent with the findings of Visioni et al. (2017b): the aerosol-driven surface cooling in G4 (contrary to G4K) favors a decreased wave activity

35   and a consequent decrease in poleward mass fluxes from the tropical reservoir, for both gas and aerosol species. On the other

hand, the increased H_2SO_4 tropical amount available for aerosol formation tends to produce larger particles with smaller equivalent optical thickness (see Niemeier and Schmidt (2017); Visioni et al. (2017c)). On light of this, smaller stratospheric heating rate anomalies are calculated in G4 with respect to G4K (Fig. 7b): in the latter case we then expect an enhanced temperature increase in the tropical lower stratosphere (Fig. 7c), coupled to a slight tropospheric warming due to SG aerosol sedimentation

5   below the tropopause. The latter, in addition, results to be greatly overbalanced by tropospheric convective cooling produced by the aerosol-driven surface cooling in G4 (contrary to G4K). As a result, the G4 atmosphere is more efficiently stabilized with respect to G4K and the positive/negative anomalies of T/u shears in the UT (Fig. 7cd) favor a decrease of TKE (and updraft velocities) in G4 with respect to G4K (Fig. 5).

All features of SW and LW heating rate anomalies in Fig. 7b can be fully explained taking into account the aerosol-O_3 coupled

10   effects (Pitari et al. (2014)). The sign of tropical ozone changes under SG conditions depends on altitude: O_3 decreases below $\sim$25 km and increases above this height: this helps explain the positive/negative heating anomalies in SW and LW components above 25 km altitude.
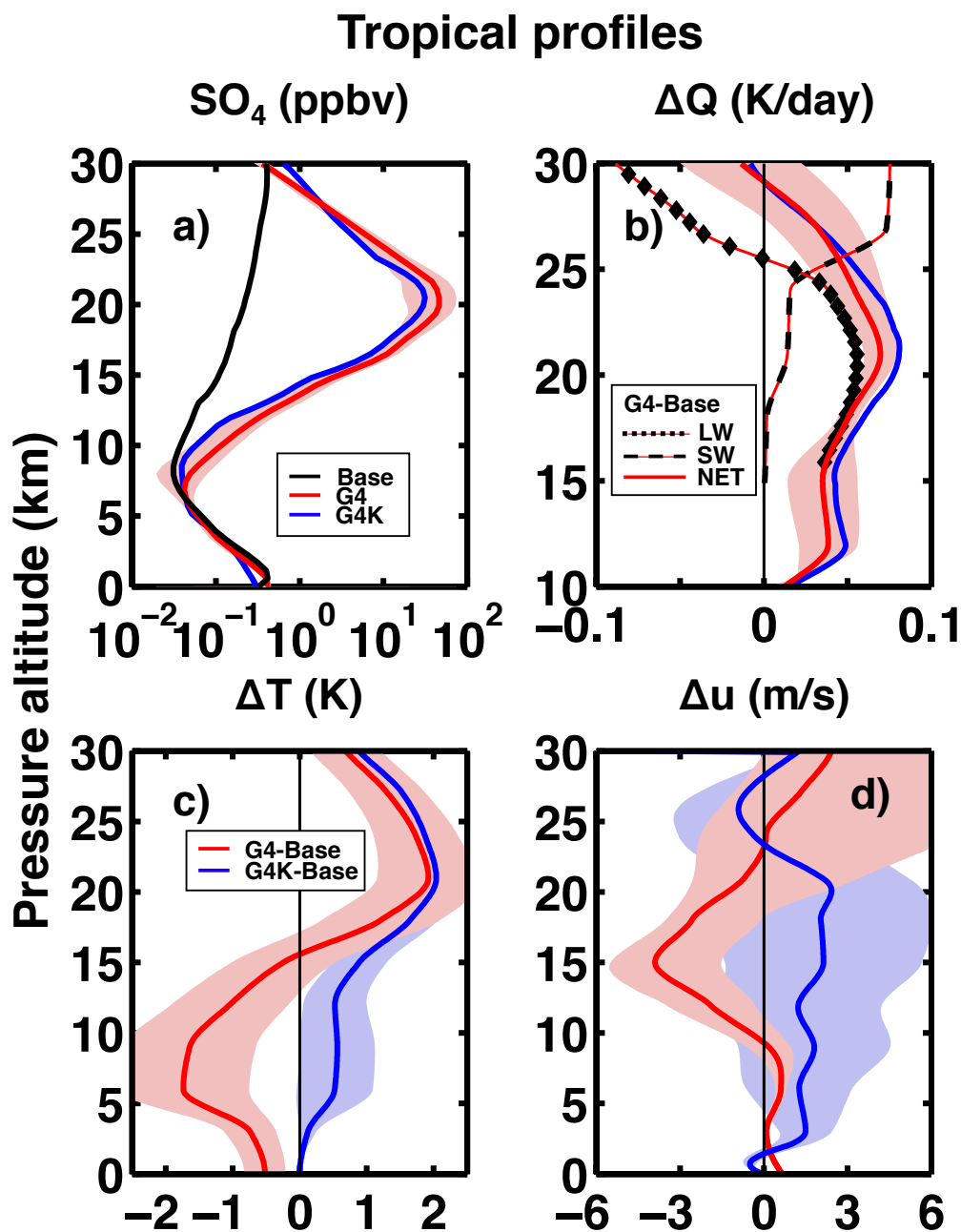
Figure 7. Average tropical vertical profiles (25S-25N, years 2030-39) of: SO$_4$ volume mixing ratio for G4, G4K and Base experiments (ppbv, panel a); G4-Base changes of net, shortwave and longwave heating rates (K/day, panel b) (LW is calculated with temperature fixed at Base values) (net heating rate changes are also shown for G4K-Base, with blue line); G4-Base and G4K-Base temperature changes (K, panel c); G4-Base and G4K-Base changes of mean zonal winds (m/s, panel d). Shaded areas of the same color represent ± 1 σ for the ensemble over the 10 year period 2030-39.

2.2 Upper tropospheric ice particles

Formation of UT ice particles is parameterized in the ULAQ-CCM by adopting the approach initially described in Karcher and Lohmann (2002), which assumes ice crystals formed only via homogeneous freezing of solution droplets as a function of local UT temperatures and updraft velocities, but including also the effects of a variable aerosol size distribution. As discussed above in Section 2, these updraft velocities are obtained as the sum of a dominant term related to TKE and a much smaller contribution from the large-scale tropospheric circulation (Lohmann and Karcher (2002)). Typical vertical velocity net values are on the order of 15-25 cm/s (Fig. 6) and allow formation of thin cirrus.

For the ice supersaturation ratio, we adopt a simplified probabilistic approach, starting from the knowledge of climatological frequencies of the UT relative humidity (RH$_{ICE}$), from which a mean value and a standard deviation can be calculated, assuming a normal distribution. Local ice super-saturation conditions (RH$_{ICE}$>100%) are a result of turbulent ascent and can be found in the UT. More precisely, when air is located below the tropopause (where turbulent updraft conditions may be found) and above an altitude with T<238 K (i.e., the assumed threshold for ice particle formation from water vapor freezing) the conditions for ice formation are met and we may calculate the probability that RH$_{ICE}$>1.5 (P$_{HOM}$). This represent the assumed threshold for homogeneous freezing to be activated, which is considerably higher with respect to the threshold for heterogeneous freezing to take place (RH$_{ICE}$>∼1.2) (Hendricks et al., 2011). The problem in this case is on the actual availability of solid ice nuclei, typically mineral dust transported from the surface or freshly emitted non-hydrophobic aviation BC particles from aviation. A low fraction of activated IN is suggested in the literature (0.1%), because the large majority of IN will rapidly be coated by sulfate (Hendricks et al. (2011)). Under typical UT conditions homogeneous freezing normally dominates ice particle formation, with respect to the heterogeneous freezing mechanism. However, this may not be considered a general conclusion and assumed to be valid in all thermodynamics conditions and any local atmospheric composition.

The calculated mass fraction of ice formed this way is shown in Fig. 8ac for two pressure layers, 150-200 hPa and 350-400 hPa, where the ice formation is greater in the tropics and mid-high latitudes, respectively. These calculations are compared against MERRA data (Bosilovich et al. (2017)), averaged over the same decade (Fig. 8bd). Tropical ice formation shows a strong land-ocean asymmetry, due to significantly higher P$_{HOM}$ values over land. For both pressure layers, the magnitude and spatial distribution of the ice mass fraction is comparable between ULAQ-CCM and MERRA.

While the probability of ice formation is defined this way, the number density and size of the ice particles formed this way is determined by the local temperature and vertical velocity. The lower the temperature, the faster the nucleation rate, thus more ice crystals can be formed. On the other hand, higher vertical velocities produce higher RH conditions leading to more ice crystals formed before the deposition of the water in the ice crystals reduces the RH conditions below the threshold. The spatial distribution of cirrus ice optical depth (OD) in the model is calculated as:

$$\tau_{ice} = \Delta z \sum_i \sum_j Q_{ext} \pi r_{ij}^2 n_{ij}(r) \tag{1}$$
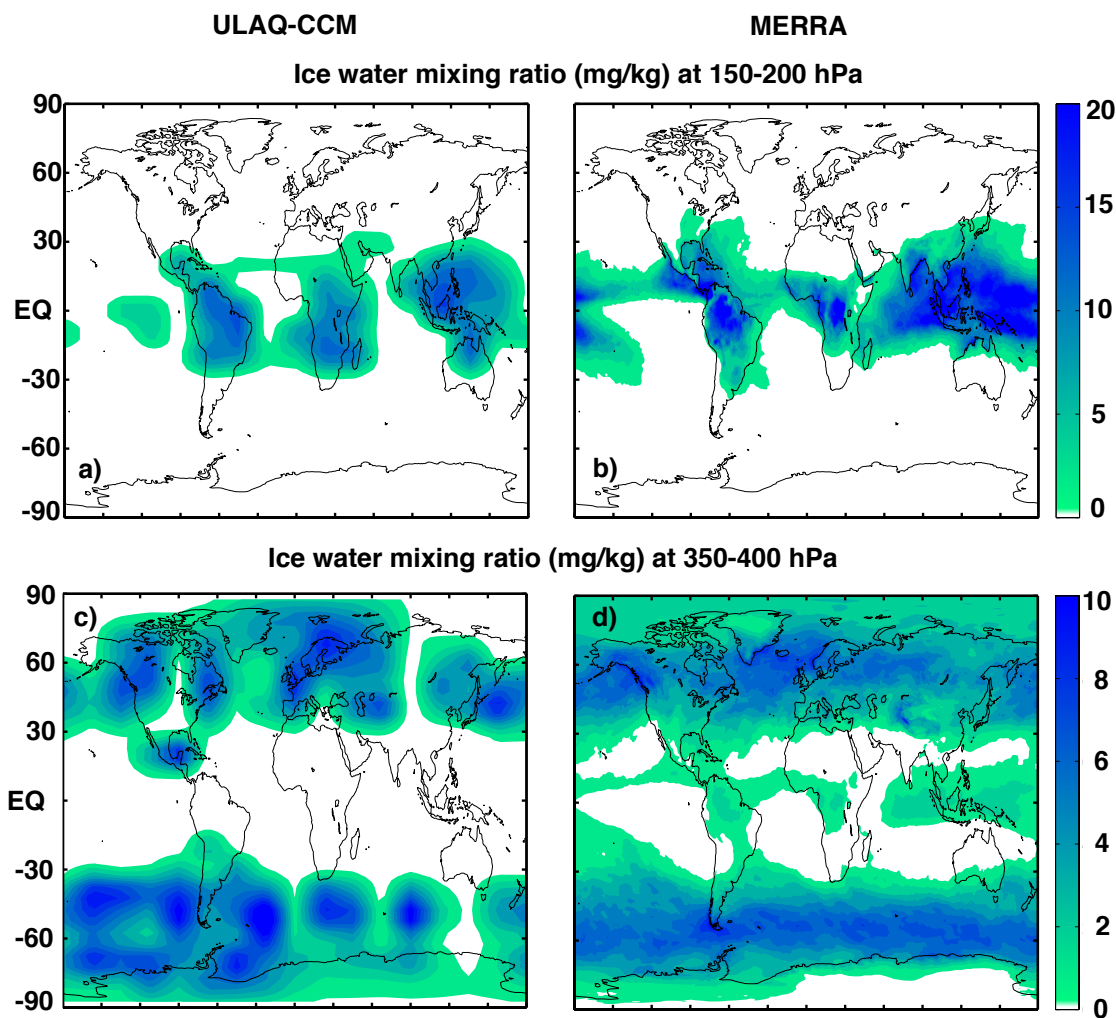
Figure 8. Lat/lon maps of ice mass fraction (mg/kg-air) for pressure layers representative of tropical (panels a,b) and extratropical (panels c,d) upper troposphere. Panels (a,c) are for the ULAQ-CCM; panels (b,d) are for MERRA data (Bosilovich et al. (2017)). Time average is on years 2003-2012.

where $Q_{ext} \sim 2$ at all visible wavelengths for ice particle sizes on the order of 5-50 μm, i is an index for the vertical layers and the sum is over all vertical layers in the UT with PHOM>0, j is an index for the particle size bins and the sum is over the whole size distribution; r_{ij}ij is the particles radius at the i-th layer and j-th bin and n_{ij} is the corresponding ice number density.

5   Eq. 1 can easily be applied in the model and the result is shown in Fig. 9a. An evaluation can be made using again the ice water mass fraction from MERRA (shown in Fig. 8bc for two specific pressure layers), together with MODIS derived values
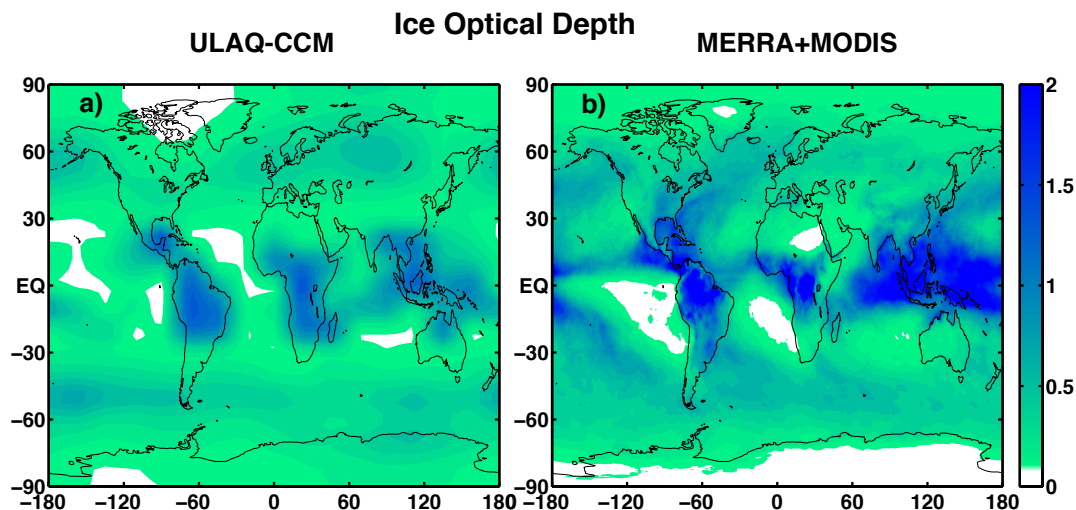
Figure 9. Ice optical depth at λ=0.55 μm, from ULAQ-CCM calculations (a) and from MERRA ice mass fractions (100 <p< 450 hPa) (Bosilovich et al. (2017)) with MODIS particle effective radius (b). Time average is on years 2003-2012 (MODIS data downloaded from https://giovanni.gsfc.nasa.gov, version MOD08M3v6).

of the ice particle effective radius (https://giovanni.gsfc.nasa.gov). With these two products we have indirectly derived τ_{ice} at every horizontal grid point in Eq. (2), using the hydrostatic equation:

$$\tau_{ice} = Q_{ext}\frac{3}{2}\frac{\Delta p}{g}\frac{1}{\rho_{ice}}\sum_i \frac{\chi_i}{r} \tag{2}$$

where the sum is again over all vertical layers (each thick Δp=50 hPa), g is the acceleration of gravity, ρ_{ice} the ice bulk
5 density, r the MODIS effective radius and χ_i the MERRA ice mass fraction at the ith layer. Doing so, we obtain an optical depth shown in Fig. 9b. The two ODs are comparable in terms of spatial distribution, with the highest values in the tropics over land. Absolute values in the ULAQ-CCM, however, result to be significantly smaller over the tropics. This should not surprise, in principle, due to the fact that we are considering only sub-visible ice clouds formed through homogeneous freezing, with a relatively narrow interval for updraft velocities (w<30 cm/s) so that events leading to thick cirrus formation are not considered.
10 In addition, ice formation from heterogeneous freezing on large IN, as mineral dust particles for example, is not taken into account in our modelling approach.
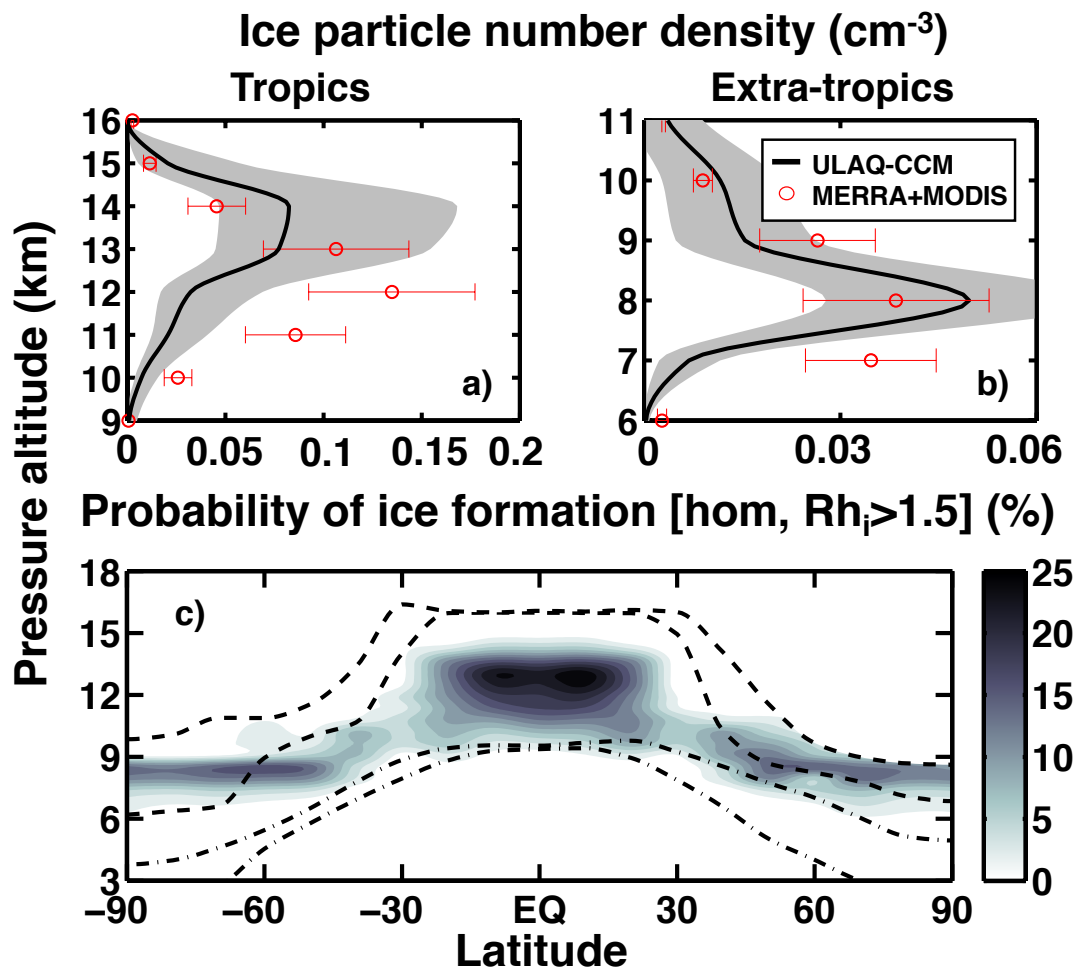
Figure 10. Average upper tropospheric profiles of ice particle number density (cm^{-3}), for the tropics (25S-25N) and extratropics (35S-90S, 35N-90N), in panels (a) and (b), respectively. The time average is on years 2003-2012. Shaded areas represent $\pm 1\sigma$ for the ensemble over the 10 year period. Red circles show indirectly derived values from MERRA ice mass fraction and MODIS effective radius (see text). Panel (c) shows the zonally averaged probability of ice formation via homogeneous freezing (percent), as a function of altitude and latitude. Dashed lines show the mean tropopause height (with seasonal variability). Dash-dotted lines show the mean height (with seasonal variability) at which the T=238 K (homogeneous freezing allowed for colder temperatures).

In Fig. 10ab we show the model calculated vertical profiles of ice particle number density averaged over the tropics (Fig. 10a) and the extra-tropics (Fig. 10b), with superimposed the time variability produced by changing conditions of vertical velocity, temperature and P_{HOM}. The ice number density maxima are located at rather different altitudes in the two latitude bands, close to 13 km in the tropics and to 8 km elsewhere. This is clearly expected from the latitudinal variability of the tropopause height.

With a procedure similar to the one described above for the ice OD, we may derive a first order approximation of the ice number density from MERRA ice mass fractions and MODIS radii. Similarly to Eq. 2, for the ice number density n_i at each vertical layer we obtain the following expression:

$$n_i = \frac{3}{4\pi} \frac{1}{\rho_{ice}} \frac{1}{r^3} \chi_i \qquad (3)$$

5   Results from Eq. 3 (red circles in Fig. 10ab) show that while the model and the indirectly derived points agree in terms of general vertical distribution and localization of the vertical maxima in the extratropics, the ULAQ-CCM tends, however, to have smaller number densities in the tropics in the 10-13 km layer. Again, this should not surprise in light of the fact that we are focusing on a specific type of cirrus cloud particles.

Figure 10c shows the model calculated values of PHOM, as a 2D zonally averaged distribution. Using these PHOM values,

10   it is possible to scale a n_i value measured in the mid-latitude airborne campaign of Strom et al. (1997) during a young cirrus formation, in order to derive an average climatological value to be considered consistent with our modeling approach. They measured a mid-latitude ice concentration value n=0.3 cm^{-3} in a young cirrus cloud at T=220 K and p=320 hPa. If we scale this result with our corresponding P$_{HOM}$=12±3%, a 'climatological-mean' value n=0.025±0.005 cm^{-3} is obtained, close to our model prediction value of 0.031± 0.008 cm^{-3} (Fig. 10b).

3 Ice perturbation due to sulfate geoengineering

In the previous section we showed that the ULAQ-CCM parametrization for ice particle formation through homogeneous freezing produces a spatial distribution of UT ice particles reasonably comparable to available data, in terms of ice number concentration, OD, mass fraction and effective radius. We now move to analyse the model calculated SG perturbation of some

5 of these quantities, by comparing G4 and G4K simulations against the Base case. As we have previously discussed and shown in Fig. 5-7, these perturbations are essentially produced and regulated by decreasing vertical velocities, (-1.7 cm/s and -0.8 cm/s, in the tropical region below the tropopause, for G4 and G4K, respectively) and by changing tropospheric temperatures (-1.2 K and +0.5 K, in the tropical UT region, for G4 and G4K, respectively).

10 The model calculated globally and time averaged size distribution of ice particles is presented in Fig. 11 for the three experiments, along with their globally averaged effective radius. A significant change in size distribution is highlighted in Fig. 11, in both SG experiments with respect to the Base case, but also between G4 and G4K. The common feature in both SG cases is the expected decreased particle population over the whole radial spectrum with respect to the Base experiment. This is due to the increased atmospheric stabilization forced by the SG aerosols, with reduced updraft velocities and consequent decrease of

15 the UT ice supersaturation probability.

The UT temperature anomalies, however, are very different in the two SG experiments with respect to the Base case (see Fig. 5). As a consequence of this, the tropospheric cooling produced in G4 by the surface temperature adjustment to the stratospheric aerosol negative RF favors a number density increase of ice particles with respect to the G4K experiment, but still less than in

20 the Base case (see also Fig. 12), due to the dominant impact of the reduced updraft. Cooler temperatures, in fact, cause faster nucleation of the ice particles, quickly removing water vapor available for the freezing itself, thus limiting the condensational growth of ice particles (Kuebbeler et al. (2012); Visioni et al. (2017a)). At the same time, velocity and temperature negative anomalies partially compensate each other also in the particle size spectrum, with a resulting effective radius in G4 larger with respect to the one in the unperturbed atmosphere (37.2 ± 4.0 μm and 32.0 ± 3.6 μm, respectively), but smaller than in G4K.

25 In this latter case, the UT is slightly warmed up respect to the Base case (see Fig. 5), so that both velocity and temperature anomalies tend to increase the particle size (39.0 ± 4.2 μm). Globally, the ULAQ-CCM baseline values of the effective radius fall well inside the MODIS range of variability (33.4 ± 2.1 μm).

As visible in Fig. 12 the calculated ice number densities follow the zonal mean behavior of the MERRA+MODIS indirectly

30 derived values, with the already discussed underestimation tendency, mainly in the tropical region (see Fig. 10).
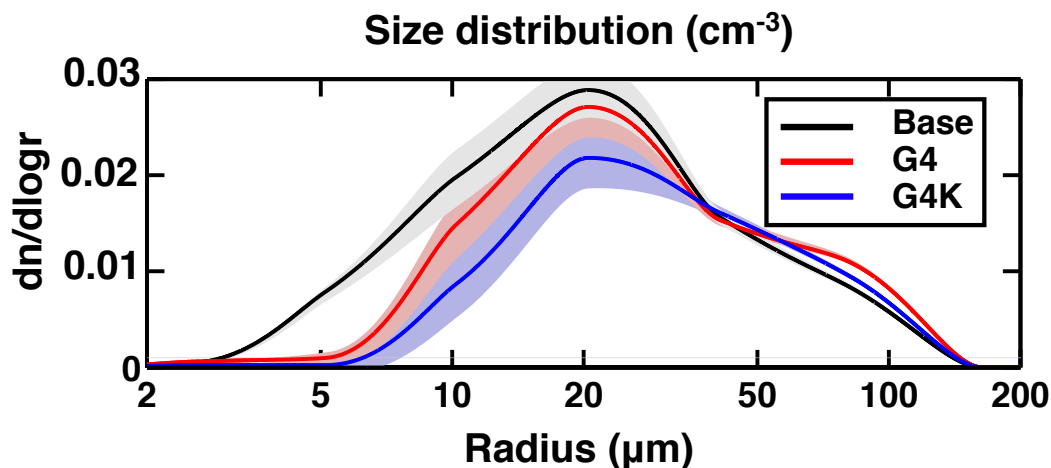
Figure 11. Globally and time averaged number density values of ice crystals as a function of particle radius (dn/dlogr, cm^{-3}) (years 2030-39). Shaded areas of the same color represent ± 1 σ for the ensemble over the 10 year period 2030-39. Calculated global mean values of the ice particle effective radius are as follows: Base $\rightarrow$ 32.0$\pm$3.6 μm; G4 $\rightarrow$ 37.2$\pm$4.0 μm; G4K $\rightarrow$ 39.0$\pm$4.2 μm. The reference MODIS value in Table 2 is 33.4$\pm$2.1 μm.
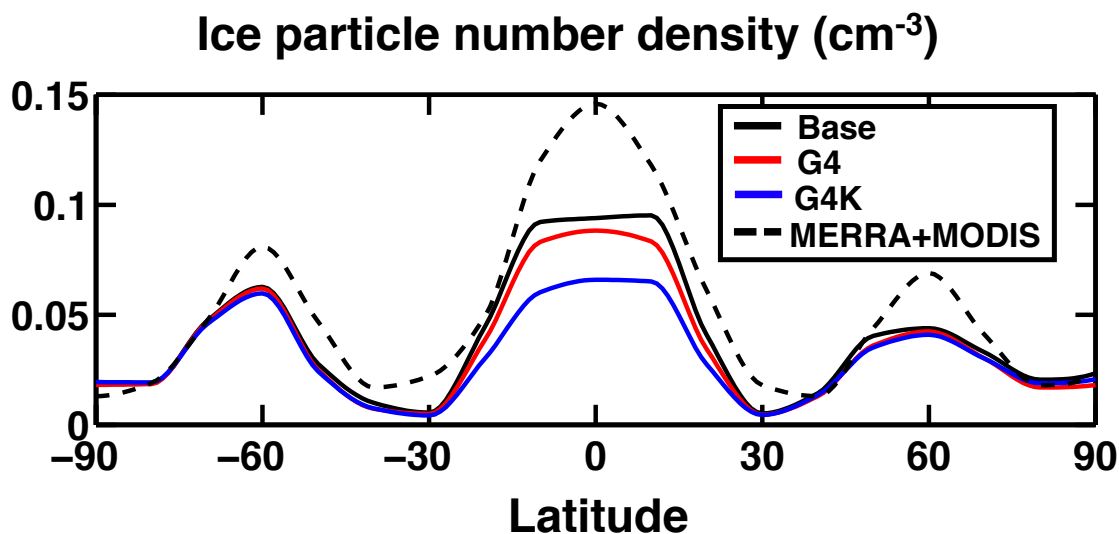
Figure 12. Zonally and time averaged total number density values of ice crystals as a function of latitude (n, cm^{-3}) (years 2030-39), as calculated in the ULAQ-CCM (for Base, G4, G4K experiments) and compared with indirectly derived values from MERRA ice mass fraction and MODIS effective radius (Eq. 3). Number densities are calculated at pressure layers 150-200 hPa for 25S-25N, 200-250 hPa for 25-35 (N/S), 250-300 hPa for 35-45 (N/S), 300-350 for 45-55 (N/S) and 350-400 for 55-90 (N/S).

3.1 Optical depth

Ice extinction anomalies G4-Base calculated in the ULAQ-CCM are negative in the whole UT (Fig. 13ab), due to the decreasing number density of the particles, caused by the reduced vertical velocities in SG dynamical conditions (see Fig. 5-6). Although the UT cooling in G4 tends to partially offset the effects of the updraft decrease on the ice particle number density, the overall

5 impact is of a general decrease of the UT ice extinction, even more pronounced than in G4K where the tropospheric cooling is not taken into account. In the latter case, however, the particle effective radius is larger than in G4, as discussed above for Fig. 11. These size distribution changes not only affect ice extinction, but also the shortwave and longwave radiative responses per unit optical depth (see ahead Section 3.2).

Following the procedure described in Section 2.2 (see Eq. 2), an evaluation of the model calculated ice extinction profiles

10 is attempted (Fig. 13cd). This is made using indirectly derived values from MERRA ice mass fraction and MODIS effective radii, as in Eq. 4 below. Here $\chi_{ext,i}$ is the ice extinction at the i-th vertical layer and $\rho_{atm,i}$ is the atmospheric mass density at the same vertical layer:

$$\chi_{ext,i} = Q_{ext} \frac{3}{2} \frac{\rho_{atm,i}}{\rho_{ice}} \frac{\chi_i}{r} \tag{4}$$

The ULAQ-CCM tropical underestimation of ice extinction below 13 km is consistent with that of the ice number density

15 and is partly justified by the specific assumptions made on cirrus cloud formation in the model, as pointed out in the discussion of Fig. 10.

The net result on ice optical depth (i.e., the vertical integral of ice extinction) is shown in Fig. 14. In general, a latitude-dependent OD reduction comparable to that found in Kuebbeler et al. (2012) is present in G4K, while in the G4 case (as

20 expected from the extinction anomalies) a further decrease is calculated mainly in the tropics, even though tropospheric temperatures are cooler. The effects regarding temperature and updraft cannot be easily separated, but the colder tropospheric temperatures in G4 with respect to G4K reduce the particle size increase respect to the Base case, producing an additional decrease in optical depth. The coupled effects of velocity and temperature anomalies on ice particle number density and size produce the most relevant impact in our study, pointing out to the importance of allowing surface temperatures to respond to

25 the stratospheric aerosol radiative forcing.
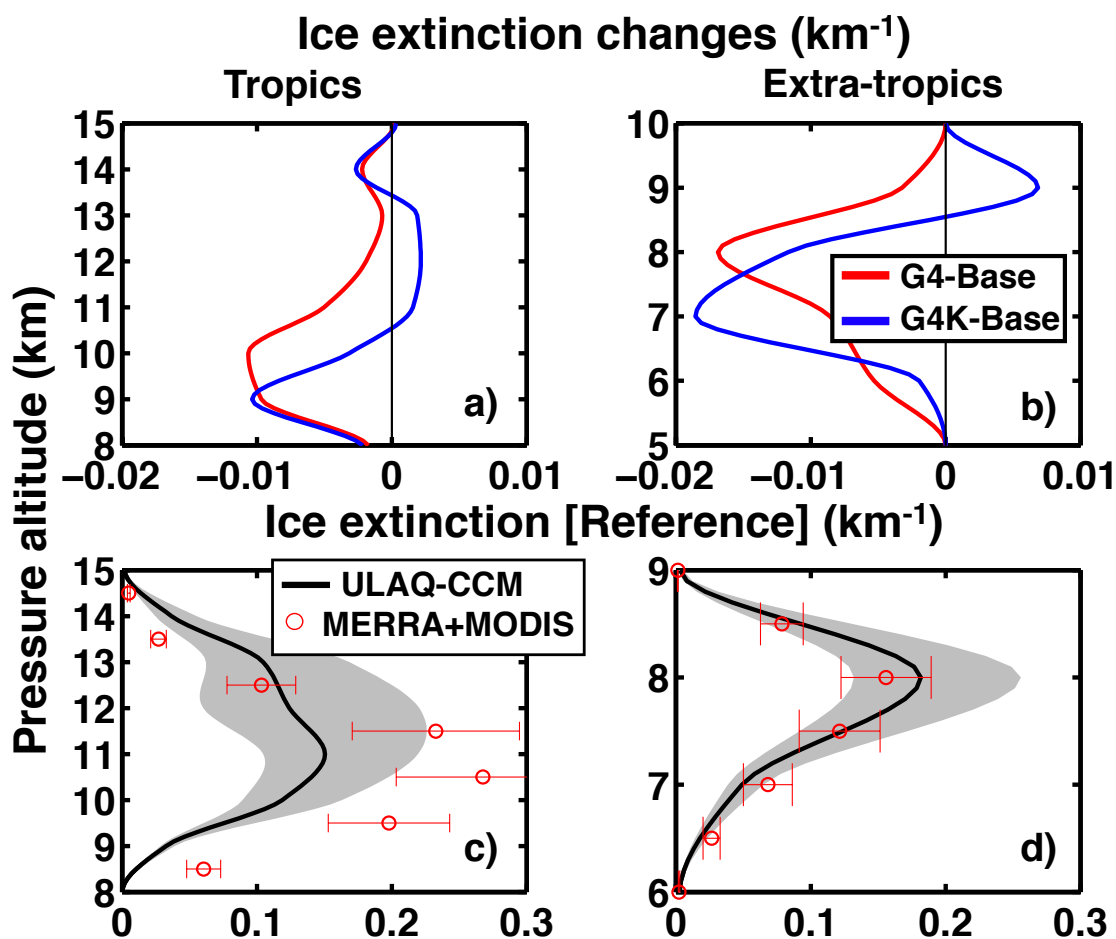
Figure 13. Average upper tropospheric profiles of ice particle extinction (λ=0.55 μm) (km-1), for the tropics (25S-25N) and extratropics (35S-90S, 35N-90N), in panels (a,c) and (b,d), respectively. Panels (a,b): ice extinction changes for G4-Base (red curves) and G4K-Base (blue curves) (years 2030-39). Panels (c,d): comparison of ULAQ-CCM calculated values of ice extinction with indirectly derived values from MERRA ice mass fraction and MODIS effective radius (red circles) (see text). Time average is on years 2003-2012. Shaded areas represent $\pm 1 \sigma$ for the ensemble over the 10 year period.
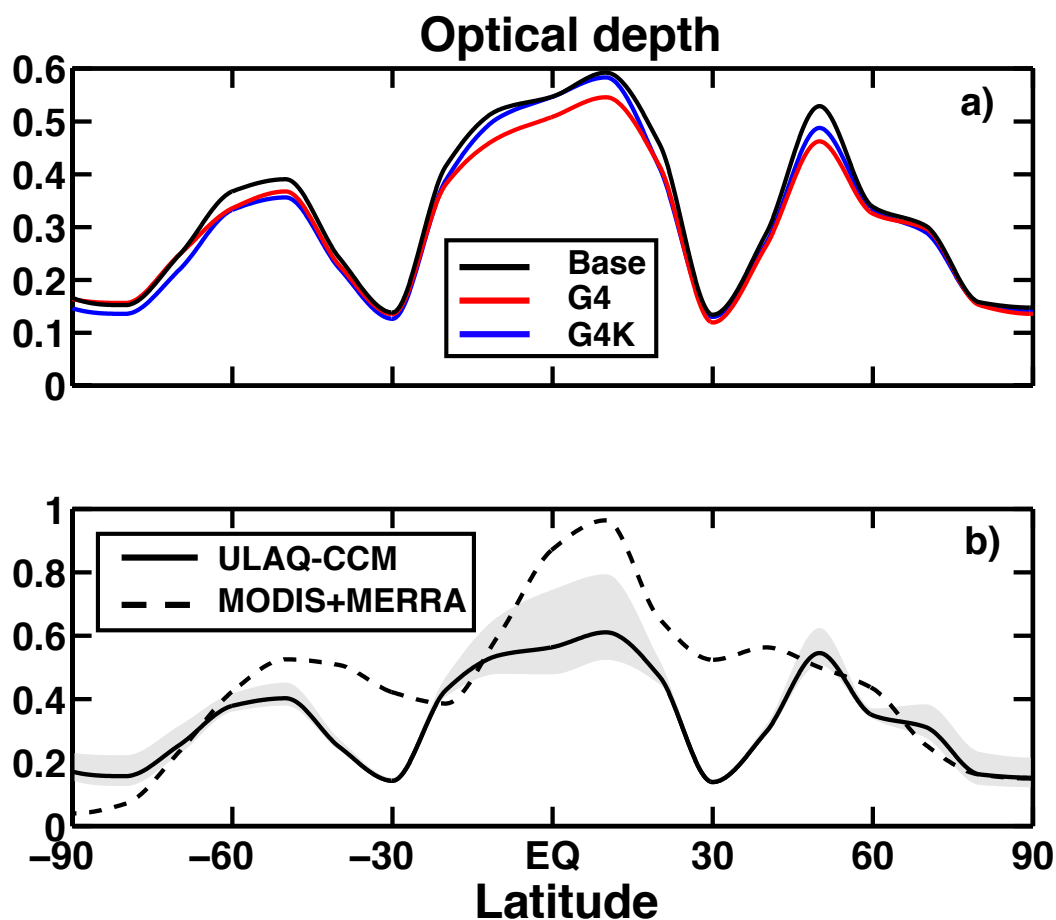
Figure 14. Zonally and time averaged values of ice optical depth (λ=0.55 μm) for ULAQ-CCM Base, G4 and G4K experiments (solid black, red and blue lines, respectively) (panel a) and Base case comparison with MERRA+MODIS indirectly derived values (dashed black line) (panel b). Model results are for years 2030-39; MERRA+MODIS data are for years 2003-12. The shaded area represents $\pm 1\ \sigma$ for the ensemble over the 10 year period 2030-39.

3.2 Radiative forcing

The well tested radiative transfer code on-line in the ULAQ-CCM (Chou (2001); Randles et al. (2013); SPARC (2013)), has been used to calculate shortwave and longwave components of the tropopause radiative forcing due to SG aerosols (direct forcing) and to UT ice changes produced by the SG-driven dynamical perturbations on the homogeneous freezing process for ice formation (indirect forcing) in Table 3. Results are shown separately for G4 and G4K experiments, both with respect to the RCP4.5 Base case. Following the above discussed thinning of UT ice clouds, a positive SW RF is calculated, because of the decreased scattering of incoming solar radiation by the ice particles. However, such an effect is largely covered by the negative LW RF due to a lessened capacity of the ice particles to trap outgoing planetary radiation, therefore the obtained net effect on RF is negative, as shown in Table 3. This indirect negative RF is smaller but of the same order of magnitude of the negative direct RF due to the increased solar radiation scattering by SG aerosols.

It is interesting to note that the shortwave component of ice RF is indeed smaller than the longwave component, but not as much one could expect from the very different normalized RFs (i.e., forcing per unit OD) at a given particle radius. The reason is that both SW and LW normalized RFs are decreasing with increasing particle radius, but the relative changes of these normalized RF components are significantly different between SW and LW. According to our radiative calculations, SW normalized values decrease (in magnitude) from -12.1 W/m^2 to -5.7 W/m^2 (-53%) with the ice effective radius increasing from 15 μm to 40 μm, whereas the LW normalized RF values remain quasi-constant on average value +53 W/m^2, with a smooth 3% decrease over the same radius interval. The resulting SW RF is then controlled not only by the negative OD changes (-0.030 in G4 and -0.020 G4K), but also by the magnitude of the particle radius increase, which is larger in G4K than in G4, both with respect to the Base case (see above discussion of Fig. 11).

Table 3. Top three rows: globally and time averaged values of upper tropospheric ice optical depth changes and RF differences (W/m^2) between the SG perturbed experiments and the RCP4.5 Base case, due to changes in ice crystal concentration and size. Middle three rows: globally averaged values of stratospheric sulfate aerosol optical depth changes and RF differences (W/m^2) defined as above, due to changes in aerosol concentration and size. Bottom three rows: total OD and RF changes (i.e., ice + sulfate). All results are for all-sky conditions (i.e., including presence of background cloudiness) and with 8 Tg-SO$_2$/yr injection. RFs are calculated at the tropopause with adjustment of stratospheric temperatures. Time average is on years 2030-39.

Exp [all sky]	Ice OD change	RF SW	RF LW	RF Net
G4-Base	-0.030	+0.75	-1.71	-0.96
G4K-Base	-0.020	+0.81	-1.02	-0.21
Exp [all sky]	SO$_4$ OD change	RF SW	RF LW	RF Net
G4-Base	+0.079	-2.03	+0.86	-1.17
G4K-Base	+0.083	-2.14	+0.90	-1.24
Exp [all sky]	Total OD change	RF SW	RF LW	RF Net
G4-Base	-0.030+0.079	-1.28	-0.85	-2.13
G4K-Base	-0.020+0.083	-1.33	-0.12	-1.45

Table 4. Rearrangement of the results presented in Table 3, with the calculated cloud adjustments (bottom three rows) in clear-sky RF components (top three rows). Cloud adjustments for SW and LW RF contributions are shown separately for the mere presence of background atmospheric clouds (left) and for the cirrus thinning (right): the former is calculated as the difference between all-sky and clear-sky aerosol RFs, with all-sky including background warm clouds and fixed UT ice clouds.

Exp [clear sky]	RF SW		RF LW		RF Net
G4-Base	-3.13		+1.07		-2.06
G4K-Base	-3.30		+1.14		-2.16
Cloud adjustment	RF SW		RF LW		RF Net
G4-Base	+1.10	+0.75	-0.21	-1.71	-0.07
G4K-Base	+1.16	+0.81	-0.24	-1.02	+0.71

Table 4 presents in a compact form the globally and time averaged ULAQ-CCM results for the cloud adjustments of clear-sky RF components due to SG stratospheric aerosols. SW and LW cloud adjustments are roughly comparable to the ones calculated in Kuebbeler et al. (2012) (+1.11 W/m^2 and -0.51 W/m^2, respectively, calculated at the top of atmosphere for a SG experiment with 5 Tg-SO$_2$/yr injection). These numbers could be directly compared with those obtained in the ULAQ-CCM G4K case, if a 5/8 scaling of the total RF results is made (as a rough first approximation). Following this procedure, we obtain SW and LW cloud adjustments of +1.23 W/m^2 and -0.79 W/m^2, respectively, for the 'scaled G4K experiment', with a net value of +0.44 W/m^2, against +0.60 W/m^2 in Kuebbeler et al. (2012).

In the (more realistic) G4 simulation performed by the ULAQ-CCM model, the SW cloud adjustment is only a bit smaller than in G4K, while a much larger negative LW component is calculated. This ends up in a net adjustment of -0.07 W/m^2 in G4 against +0.71 W/m^2 in the G4K experiment. A latitude-dependent view of these results is presented in Fig. 15. The black solid line shows the net positive adjustment (SW+LW) due to the mere presence of background clouds, whose increased reflectivity

5   enhances the downward scattered solar radiation by the stratospheric aerosol layer. According to our model calculations, the negative LW is the dominant component of the cloud adjustment due to cirrus ice thinning, and this is particularly true for the more realistic G4 simulation. In this latter case, significantly larger values of the LW adjustment are found over the tropics with respect to G4K, consistently with the ice extinction profile changes in Fig. 13a.
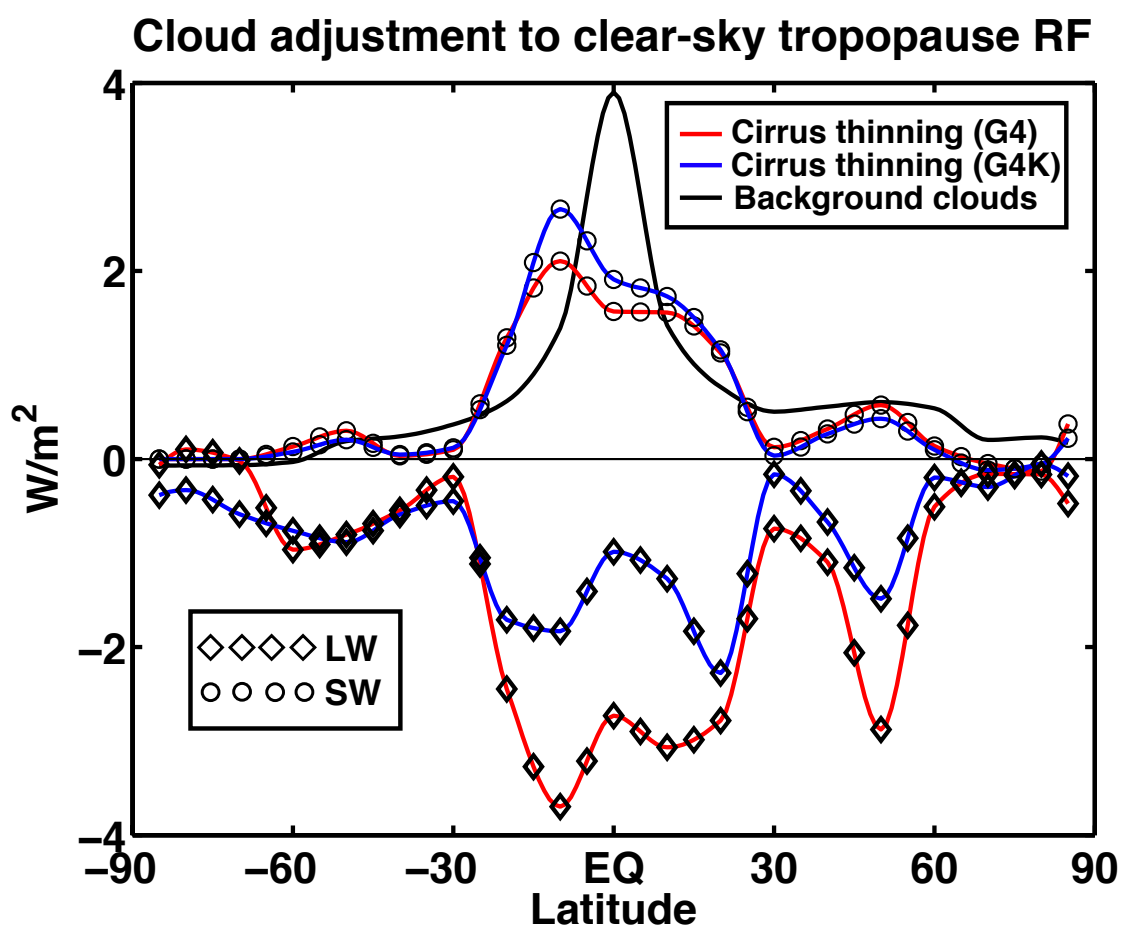
Figure 15. Cloud adjustments in clear-sky SG aerosol RF (W/m^2). See legends for line meaning. The positive adjustment due to (passive) background clouds (black solid line) shows the net value (SW+LW), which is however largely controlled by the SW contribution (see Table 4).

4 Conclusions

Sulfate geoengineering is considered, amongst other solar radiation management (SRM) techniques, one of the most promising. One reason for this (and unlike other methods) is that we have a natural proxy for the stratospheric sulfate injection, i.e., past explosive volcanic eruptions in the tropical belt. This does not mean that SG does not still pose some scientific questions that

5 need to be answered thoroughly, as pointed out by MacMartin et al. (2016). For instance, models still show many significant differences regarding the confinement of stratospheric sulfate aerosols in the tropical pipe Pitari et al. (2014).

In recent years some experiments have been proposed where SG is used to meet different climate targets (MacMartin et al. (2017); Kravitz et al. (2017)). However, to properly do so, a clear understanding is needed of how multiple side effects of this technique can modify the net RF (Visioni et al., 2017a). While some of these effects produce a negligible difference in forcing,

10 such as those from gas species perturbations (CH_4, O_3, stratospheric H_2O) (Visioni et al. (2017b)), this might not be the case for changes produced in the formation of thin cirrus ice clouds.

This latter indirect effect was already analyzed in two previous works: Cirisan et al. (2013) looked at the potential impact of IN changes in the UT, finding a negligible positive TOA forcing (+0.02 W/m^2, up to 0.04 W/m^2) due to the number density increase of H_2SO_4-H_2O aerosols transported down in the UT from the lower stratosphere. Kuebbeler et al. (2012), on the

15 other hand, have studied the effects of dynamical changes caused by the aerosol induced stratospheric warming and their consequences on UT ice formation via homogeneous freezing.They found a considerable negative TOA forcing in the longwave spectrum (-0.51 W/m^2), greatly attributable to the SG-induced ice optical depth reduction. In the present study, we focused on these same indirect dynamical effects, adding the potential impact of the SG aerosol induced surface cooling (G4 experiment), which was not explicitly considered in the study of Kuebbeler et al. (2012). Their approach was also included for comparison

20 in our study, by means of a sensitivity study (G4K) conducted with the ULAQ-CCM, where we keep the surface temperature fixed at the RCP4.5 baseline values, so that we could quantify more precisely the surface cooling impact on UT thin cirrus clouds.

A compact view of the surface cooling effects on UT ice formation was presented in Fig. 2. On one hand, the aerosol induced stratospheric warming and surface cooling combined together, produce a further atmospheric stabilization with an even larger

25 reduction in tropospheric updraft with respect to the G4K case. This lowers the UT probability for ice supersaturation and thus less favorable conditions for homogeneous freezing. On the other hand, this ice formation limiting effect is partially counterbalanced by the convectively-driven tropospheric cooling, which is not observed in the G4K case.

The resulting changes in ice particle number density and size distribution, when combined, translate into a globally averaged decrease of ice optical depth ($\Delta\tau$=-0.030, at λ=0.55 μm), i.e., -7.5% of the baseline OD. This reduction is larger than the one

30 in G4K relative to the Base case ($\Delta\tau$=-0.020, -5%), pointing out to the dominant and controlling role of the reduced updraft velocities. According to our model results, these OD changes (coupled to increases in ice particle effective radii) translate in net tropopause RFs of -0.96 W/m^2 and -0.21 W/m^2, for G4 and G4K experiments, respectively, produced only by the cirrus ice thinning effect of SG. These two cloud adjustments result from a combination of SW and LW RF contributions, that account for +0.75 W/m^2 and +0.81 W/m^2 in the SW (for G4 and G4K, respectively) and -1.71 W/m^2 and -1.02 W/m^2 in the LW (again

for G4 and G4K).

We can compare these ice thinning forcing contributions with the net tropopause all-sky RF produced by the stratospheric SG aerosols, i.e., of -1.17 W/m^2 and -1.24 W/m^2, for G4 and G4K experiments, respectively: according to our model, the net negative RF due to the cirrus ice cloud thinning, is (in G4) of the same order of magnitude of the direct effect of the sulfate

5   particles themselves. This might have consequences in the definition of the sulfate injection efficiency in terms of RF per Tg-S injected, especially if such efficiency is used to determine the amount of SO$_2$ that needs to be injected in the stratosphere to achieve climate targets (MacMartin et al. (2017); Kravitz et al. (2017)).

Furthermore, one last consideration is necessary regarding RFs in SG scenarios and the unperturbed atmosphere; more specifically, regarding the cloud adjustment to clear-sky RFs due to the stratospheric sulfate aerosols. In our fully interactive aerosol

10   simulation (G4), we obtain a total cloud adjustment (from both cirrus ice thinning and passive background clouds) close to zero (-0.07 W/m^2), due to compensating large adjustments in the LW and SW. The SW adjustment results in part from the mere presence of (passive) background clouds and in part from the changing size distribution of UT ice particles. The increasing particle size is more pronounced in the partially interactive aerosol simulation (G4K), thus producing a larger positive SW contribution, with a consequent net positive cloud adjustment (+0.71 W/m^2).

15   This latter value is fully comparable to the one calculated in the similar experiment of Kuebbeler et al. (2012) (+0.60 W/m^2, with a 5 Tg-SO$_2$ injection). It means that the lower stratospheric warming produced by SG aerosols acts indirectly on atmospheric dynamics with a strong feedback on UT cirrus clouds, so that a simple reduction of the incoming solar radiation is not a good proxy for the eventual injection of sulfate particles in the stratosphere. When the aerosol induced surface cooling is coupled to the lower stratospheric warming, the net cloud adjustment is significantly reduced; however, the clear-sky balance

20   of SW and LW RF contributions is greatly altered by the presence of background clouds coupled to the UT ice thinning.

One important caveat to the conclusions of this study, is that the physical processes behind UT ice particle formation are highly idealized in our parameterization. Nonetheless, the results it produces in the reference (historical) simulation are generally comparable with MERRA reanalysis and some satellite data. In addition, the calculated SG dynamical anomalies in the stratosphere are consistent with those from other modeling studies (Pitari et al. (2014); Niemeier and Schmidt (2017)). Finally,

25   taking into account the consistency with findings from the study of Kuebbeler et al. (2012), we may reasonably conclude that our results regarding the thinning of UT ice clouds under SG conditions are sufficiently robust. However, considering how complex is the balance between UT ice formation changes and their radiative forcing (Sanderson et al. (2008); Mitchell et al. (2008)), the results in the present cannot be considered conclusive and exhaustive. Additional results using different and more complete physical parametrizations (both regarding the ice formation processes and a wider range of updraft velocities),

30   together with an on-line ocean coupling, may help clarify the net contribution of ice clouds in a sulfate geoengineering scenario.

Acknowledgements. Some of the analyses and visualizations used in this study were produced with the Giovanni online data system, developed and maintained by the NASA GES DISC. We also acknowledge the MODIS mission scientists and associated NASA personnel for the production of the data used in this research effort. We thank Simone Tilmes (NCAR) for providing surface temperature data from the atmosphere-ocean coupled model CCSM-CAM4, to be used in the ULAQ-CCM numerical simulations. One of the authors (GP) would like to thank Bernd Karcher for helpful discussions on the physical processes behind aerosol-ice interactions and for providing the heterogeneous freezing numerical code used in the ULAQ-CCM.

References

Aquila, V., Garfinkel, C., Newman, P., Oman, L., and Waugh, D.: Modifications of the quasi-biennial oscillation by a geoengineering perturbation of the stratospheric aerosol layer, Geophysical Research Letters, 41, 1738–1744, 2014.

Bosilovich, M. G., Robertson, F. R., Takacs, L., Molod, A., and Mocko, D.: Atmospheric Water Balance and Variability in the MERRA-2
5   Reanalysis, Journal of Climate, 30, 1177–1196, doi:10.1175/JCLI-D-16-0338.1, https://doi.org/10.1175/JCLI-D-16-0338.1, 2017.

Budyko, M. I.: The Climate of the Future, American Geophysical Union, doi:10.1002/9781118665251.ch7, http://dx.doi.org/10.1002/9781118665251.ch7, 1974.

Canty, T., Mascioli, N. R., Smarte, M. D., and Salawitch, R. J.: An empirical model of global climate - Part 1: A critical evaluation of volcanic cooling, Atmospheric Chemistry and Physics, 13, 3997–4031, doi:10.5194/acp-13-3997-2013, http://www.atmos-chem-phys.
10   net/13/3997/2013/, 2013.

Chen, T., Zhang, Y., and Rossow, W. B.: Sensitivity of Atmospheric Radiative Heating Rate Profiles to Variations of Cloud Layer Overlap, Journal of Climate, 13, 2941–2959, doi:10.1175/1520-0442(2000)013<2941:SOARHR>2.0.CO;2, https://doi.org/10.1175/1520-0442(2000)013<2941:SOARHR>2.0.CO;2, 2000.

Chipperfield, M. P., Liang, Q., Strahan, S. E., Morgenstern, O., Dhomse, S. S., Abraham, N. L., Archibald, A. T., Bekki, S., Braesicke, P.,
15   Di Genova, G., Fleming, E. L., Hardiman, S. C., Iachetti, D., Jackman, C. H., Kinnison, D. E., Marchand, M., Pitari, G., Pyle, J. A., Rozanov, E., Stenke, A., and Tummon, F.: Multimodel estimates of atmospheric lifetimes of long-lived ozone-depleting substances: Present and future, Journal of Geophysical Research: Atmospheres, 119, 2555–2573, doi:10.1002/2013JD021097, http://dx.doi.org/10.1002/2013JD021097, 2014.

Chou, M. M. J. S. X. L.: A thermal infrared radiation parameterization for atmospheric studies, Tech. Rep. TM-2001-104606, NASA, NASA
20   Goddard Space Flight Cent., Greenbelt, MD, 2001.

Cirisan, A., Spichtinger, P., Luo, B. P., Weisenstein, D. K., Wernli, H., Lohmann, U., and Peter, T.: Microphysical and radiative changes in cirrus clouds by geoengineering the stratosphere, Journal of Geophysical Research: Atmospheres, 118, 4533–4548, doi:10.1002/jgrd.50388, http://dx.doi.org/10.1002/jgrd.50388, 2013.

Clegg, S. M. and Abbatt, J. P. D.: Oxidation of SO$_2$ by H$_2$O$_2$ on ice surfaces at 228 K: a sink for SO$_2$ in ice clouds, Atmospheric Chemistry
25   and Physics, 1, 73–78, doi:10.5194/acp-1-73-2001, https://www.atmos-chem-phys.net/1/73/2001/, 2001.

Crutzen, P. J.: Albedo Enhancement by Stratospheric Sulfur Injections: A Contribution to Resolve a Policy Dilemma?, Climatic Change, 77, 211–220, doi:10.1007/s10584-006-9101-y, http://dx.doi.org/10.1007/s10584-006-9101-y, 2006.

Eyring, V., Butchart, N., Waugh, D. W., Akiyoshi, H., Austin, J., Bekki, S., Bodeker, G. E., Boville, B. A., Bruhl, C., Chipperfield, M. P., Cordero, E., Dameris, M., Deushi, M., Fioletov, V. E., Frith, S. M., Garcia, R. R., Gettelman, A., Giorgetta, M. A., Grewe, V., Jourdain, L.,
30   Kinnison, D. E., Mancini, E., Manzini, E., Marchand, M., Marsh, D. R., Nagashima, T., Newman, P. A., Nielsen, J. E., Pawson, S., Pitari, G., Plummer, D. A., Rozanov, E., Schraner, M., Shepherd, T. G., Shibata, K., Stolarski, R. S., Struthers, H., Tian, W., and Yoshiki, M.: Assessment of temperature, trace species, and ozone in chemistry-climate model simulations of the recent past, Journal of Geophysical Research: Atmospheres, 111, n/a–n/a, doi:10.1029/2006JD007327, d22308, 2006.

Feichter, J., Kjellstram, E., Rodhe, H., Dentener, F., Lelieveldi, J., and Roelofs, G.-J.: Simulation of the tropospheric sulfur cycle in a global
35   climate model, Atmospheric Environment, 30, 1693 – 1707, doi:https://doi.org/10.1016/1352-2310(95)00394-0, http://www.sciencedirect.com/science/article/pii/1352231095003940, joint 8th CAGCP and 2nd IGAC Conference on Global Atmospheric Chemistry, 1996.

Fusina, F., Spichtinger, P., and Lohmann, U.: Impact of ice supersaturated regions and thin cirrus on radiation in the midlatitudes, Journal of Geophysical Research: Atmospheres, 112, n/a–n/a, doi:10.1029/2007JD008449, http://dx.doi.org/10.1029/2007JD008449, d24S14, 2007.

Gasparini, B., Munch, S., Poncet, L., Feldmann, M., and Lohmann, U.: Is increasing ice crystal sedimentation velocity in geoengineering simulations a good proxy for cirrus cloud seeding?, Atmospheric Chemistry and Physics, 17, 4871–4885, doi:10.5194/acp-17-4871-2017,
5   https://www.atmos-chem-phys.net/17/4871/2017/, 2017.

Gettelman, A., Liu, X., Ghan, S. J., Morrison, H., Park, S., Conley, A. J., Klein, S. A., Boyle, J., Mitchell, D. L., and Li, J.-L. F.: Global simulations of ice nucleation and ice supersaturation with an improved cloud scheme in the Community Atmosphere Model, Journal of Geophysical Research: Atmospheres, 115, n/a–n/a, doi:10.1029/2009JD013797, http://dx.doi.org/10.1029/2009JD013797, d18216, 2010.

Hegglin, M. I., Gettelman, A., Hoor, P., Krichevsky, R., Manney, G. L., Pan, L. L., Son, S.-W., Stiller, G., Tilmes, S., Walker, K. A., Eyring,
10   V., Shepherd, T. G., Waugh, D., Akiyoshi, H., Anel, J. A., Austin, J., Baumgaertner, A., Bekki, S., Braesicke, P., Bruhl, C., Butchart, N., Chipperfield, M. P., Dameris, M., Dhomse, S., Frith, S., Garny, H., Hardiman, S. C., Jockel, P., Kinnison, D. E., Lamarque, J. F., Mancini, E., Michou, M., Morgenstern, O., Nakamura, T., Olivie, D., Pawson, S., Pitari, G., Plummer, D. A., Pyle, J. A., Rozanov, E., Scinocca, J. F., Shibata, K., Smale, D., Teyssedre, H., Tian, W., and Yamashita, Y.: Multimodel assessment of the upper troposphere and lower stratosphere: Extra-tropics, Journal of Geophysical Research: Atmospheres, 115, D00M09, doi:10.1029/2010JD013884, https:
15   //hal.archives-ouvertes.fr/hal-00510687, 2010.

Hendricks, J., Karcher, B., and Lohmann, U.: Effects of ice nuclei on cirrus clouds in a global climate model, Journal of Geophysical Research: Atmospheres, 116, doi:10.1029/2010JD015302, http://dx.doi.org/10.1029/2010JD015302, d18206, 2011.

Karcher, B. and Lohmann, U.: A parameterization of cirrus cloud formation: Homogeneous freezing of supercooled aerosols, Journal of Geophysical Research: Atmospheres, 107, doi:10.1029/2001JD000470, http://dx.doi.org/10.1029/2001JD000470, 2002.

20   Kleinschmitt, C., Boucher, O., and Platt, U.: Sensitivity of the radiative forcing by stratospheric sulfur geoengineering to the amount and strategy of the SO_2 injection studied with the LMDZ-S3A model, Atmospheric Chemistry and Physics Discussions, 2017, 1–34, doi:10.5194/acp-2017-722, https://www.atmos-chem-phys-discuss.net/acp-2017-722/, 2017.

Kravitz, B., Robock, A., Boucher, O., Schmidt, H., Taylor, K. E., Stenchikov, G., and Schulz, M.: The Geoengineering Model Intercomparison Project (GeoMIP), Atmospheric Science Letters, 12, 162–167, doi:10.1002/asl.316, http://dx.doi.org/10.1002/asl.316, 2011.

25   Kravitz, B., Robock, A., and Irvine, P.: Robust Results From Climate Model Simulations of Geoengineering, Eos, Transactions American Geophysical Union, 94, 292–292, doi:10.1002/2013EO330005, http://dx.doi.org/10.1002/2013EO330005, 2013.

Kravitz, B., MacMartin, D. G., Mills, M. J., Richter, J. H., Tilmes, S., Lamarque, J.-F., Tribbia, J. J., and Vitt, F.: First Simulations of Designing Stratospheric Sulfate Aerosol Geoengineering to Meet Multiple Simultaneous Climate Objectives, Journal of Geophysical Research: Atmospheres, 122, 12,616–12,634, doi:10.1002/2017JD026874, http://dx.doi.org/10.1002/2017JD026874, 2017JD026874, 2017.

30   Kuebbeler, M., Lohmann, U., and Feichter, J.: Effects of stratospheric sulfate aerosol geo-engineering on cirrus clouds, Geophysical Research Letters, 39, doi:10.1029/2012GL053797, http://dx.doi.org/10.1029/2012GL053797, l23803, 2012.

Lohmann, U. and Karcher, B.: First interactive simulations of cirrus clouds formed by homogeneous freezing in the ECHAM general circulation model, Journal of Geophysical Research: Atmospheres, 107, AAC 8–1–AAC 8–13, doi:10.1029/2001JD000767, http://dx.doi.org/10.1029/2001JD000767, 2002.

35   Long, C. S. and Stowe, L. L.: using the NOAA/AVHRR to study stratospheric aerosol optical thicknesses following the Mt. Pinatubo Eruption, Geophysical Research Letters, 21, 2215–2218, doi:10.1029/94GL01322, http://dx.doi.org/10.1029/94GL01322, 1994.

MacMartin, D. G., Kravitz, B., Long, J. C. S., and Rasch, P. J.: Geoengineering with stratospheric aerosols: What do we not know after a decade of research?, Earth's Future, 4, 543–548, doi:10.1002/2016EF000418, http://dx.doi.org/10.1002/2016EF000418, 2016EF000418, 2016.

MacMartin, D. G., Kravitz, B., Tilmes, S., Richter, J. H., Mills, M. J., Lamarque, J.-F., Tribbia, J. J., and Vitt, F.: The Climate Response to Stratospheric Aerosol Geoengineering Can Be Tailored Using Multiple Injection Locations, Journal of Geophysical Research: Atmospheres, 122, 12,574–12,590, doi:10.1002/2017JD026868, http://dx.doi.org/10.1002/2017JD026868, 2017JD026868, 2017.

Mitchell, D. L., Rasch, P., Ivanova, D., McFarquhar, G., and Nousiainen, T.: Impact of small ice crystal assumptions on ice sedimentation rates in cirrus clouds and GCM simulations, Geophysical Research Letters, 35, n/a–n/a, doi:10.1029/2008GL033552, http://dx.doi.org/10.1029/2008GL033552, l09806, 2008.

Morgenstern, O., Giorgetta, M. A., Shibata, K., Eyring, V., Waugh, D. W., Shepherd, T. G., Akiyoshi, H., Austin, J., Baumgaertner, A. J. G., Bekki, S., Braesicke, P., Bruhl, C., Chipperfield, M. P., Cugnet, D., Dameris, M., Dhomse, S., Frith, S. M., Garny, H., Gettelman, A., Hardiman, S. C., Hegglin, M. I., Jockel, P., Kinnison, D. E., Lamarque, J.-F., Mancini, E., Manzini, E., Marchand, M., Michou, M., Nakamura, T., Nielsen, J. E., Olivie, D., Pitari, G., Plummer, D. A., Rozanov, E., Scinocca, J. F., Smale, D., Teyssedre, H., Toohey, M., Tian, W., and Yamashita, Y.: Review of the formulation of present-generation stratospheric chemistry-climate models and associated external forcings, Journal of Geophysical Research: Atmospheres, 115, n/a–n/a, doi:10.1029/2009JD013728, http://dx.doi.org/10.1029/2009JD013728, d00M02, 2010.

Morgenstern, O., Hegglin, M. I., Rozanov, E., O'Connor, F. M., Abraham, N. L., Akiyoshi, H., Archibald, A. T., Bekki, S., Butchart, N., Chipperfield, M. P., Deushi, M., Dhomse, S. S., Garcia, R. R., Hardiman, S. C., Horowitz, L. W., Jockel, P., Josse, B., Kinnison, D., Lin, M., Mancini, E., Manyin, M. E., Marchand, M., Marecal, V., Michou, M., Oman, L. D., Pitari, G., Plummer, D. A., Revell, L. E., Saint-Martin, D., Schofield, R., Stenke, A., Stone, K., Sudo, K., Tanaka, T. Y., Tilmes, S., Yamashita, Y., Yoshida, K., and Zeng, G.: Review of the global models used within phase 1 of the Chemistry–Climate Model Initiative (CCMI), Geoscientific Model Development, 10, 639–671, doi:10.5194/gmd-10-639-2017, https://www.geosci-model-dev.net/10/639/2017/, 2017.

Niemeier, U. and Schmidt, H.: Changing transport processes in the stratosphere by radiative heating of sulfate aerosols, Atmospheric Chemistry and Physics, 17, 14 871–14 886, doi:10.5194/acp-17-14871-2017, https://www.atmos-chem-phys.net/17/14871/2017/, 2017.

Niemeier, U. and Tilmes, S.: Sulfur injections for a cooler planet, Science, 357, 246–248, doi:10.1126/science.aan3317, http://science.sciencemag.org/content/357/6348/246, 2017.

Pitari, G.: A Numerical Study of the Possible Perturbation of Stratospheric Dynamics Due to Pinatubo Aerosols: Implications for Tracer Transport, Journal of the Atmospheric Sciences, 50, 2443–2461, doi:10.1175/1520-0469(1993)050<2443:ANSOTP>2.0.CO;2, https://doi.org/10.1175/1520-0469(1993)050<2443:ANSOTP>2.0.CO;2, 1993.

Pitari, G., Mancini, E., Rizi, V., and Shindell, D. T.: Impact of Future Climate and Emission Changes on Stratospheric Aerosols and Ozone, Journal of the Atmospheric Sciences, 59, 414–440, doi:10.1175/1520-0469(2002)059<0414:IOFCAE>2.0.CO;2, https://doi.org/10.1175/1520-0469(2002)059<0414:IOFCAE>2.0.CO;2, 2002.

Pitari, G., Aquila, V., Kravitz, B., Robock, A., Watanabe, S., Cionni, I., De Luca, N., Di Genova, G., Mancini, E., and Tilmes, S.: Stratospheric ozone response to sulfate geoengineering: Results from the Geoengineering Model Intercomparison Project (GeoMIP), Journal of Geophysical Research: Atmospheres, 119, 2629–2653, 2014.

Pitari, G., Cionni, I., Di Genova, G., Visioni, D., Gandolfi, I., and Mancini, E.: Impact of Stratospheric Volcanic Aerosols on Age-of-Air and Transport of Long-Lived Species, Atmosphere, 7, http://www.mdpi.com/2073-4433/7/11/149, 2016a.

Pitari, G., Di Genova, G., Mancini, E., Visioni, D., Gandolfi, I., and Cionni, I.: Stratospheric Aerosols from Major Volcanic Eruptions: A Composition-Climate Model Study of the Aerosol Cloud Dispersal and e-folding Time, Atmosphere, 7, 75, doi:10.3390/atmos7060075, http://dx.doi.org/10.3390/atmos7060075, 2016b.

Pitari, G., Visioni, D., Mancini, E., Cionni, I., Di Genova, G., and Gandolfi, I.: Sulfate Aerosols from Non-Explosive Volcanoes: Chemical-Radiative Effects in the Troposphere and Lower Stratosphere, Atmosphere, 7, doi:10.3390/atmos7070085, http://www.mdpi.com/2073-4433/7/7/85, 2016c.

Randles, C. A., Kinne, S., Myhre, G., Schulz, M., Stier, P., Fischer, J., Doppler, L., Highwood, E., Ryder, C., Harris, B., Huttunen, J., Ma, Y., Pinker, R. T., Mayer, B., Neubauer, D., Hitzenberger, R., Oreopoulos, L., Lee, D., Pitari, G., Di Genova, G., Quaas, J., Rose, F. G., Kato, S., Rumbold, S. T., Vardavas, I., Hatzianastassiou, N., Matsoukas, C., Yu, H., Zhang, F., Zhang, H., and Lu, P.: Intercomparison of shortwave radiative transfer schemes in global aerosol modeling: results from the AeroCom Radiative Transfer Experiment, Atmospheric Chemistry and Physics, 13, 2347–2379, doi:10.5194/acp-13-2347-2013, http://www.atmos-chem-phys.net/13/2347/2013/, 2013.

Robock, A.: Volcanic eruptions and climate, Reviews of Geophysics, 38, 191–219, doi:10.1029/1998RG000054, http://dx.doi.org/10.1029/1998RG000054, 2000.

Sanderson, B. M., Piani, C., Ingram, W. J., Stone, D. A., and Allen, M. R.: Towards constraining climate sensitivity by linear analysis of feedback patterns in thousands of perturbed-physics GCM simulations, Climate Dynamics, 30, 175–190, doi:10.1007/s00382-007-0280-7, https://doi.org/10.1007/s00382-007-0280-7, 2008.

Sassen, K., Wang, Z., and Liu, D.: Global distribution of cirrus clouds from CloudSat/Cloud-Aerosol lidar and infrared pathfinder satellite observations (CALIPSO) measurements, Journal of Geophysical Research: Atmospheres, 113, 2008.

SPARC: Chapter 5: Model Estimates of Lifetimes in SPARC Report on Lifetimes of Stratospheric Ozone-Depleting Substances, Their Replacements, and Related Species. Chipperfield, M. and Q. Liang, et al. , Tech. rep., SPARC, http://www.sparc-climate.org/publications/sparc-reports/, 2013.

Strom, J., Strauss, B., Anderson, T., Schrader, F., Heintzenberg, J., and Wendling, P.: In Situ Observations of the Microphysical Properties of Young Cirrus Clouds, Journal of the Atmospheric Sciences, 54, 2542–2553, doi:10.1175/1520-0469(1997)054<2542:ISOOTM>2.0.CO;2, http://dx.doi.org/10.1175/1520-0469(1997)054<2542:ISOOTM>2.0.CO;2, 1997.

Taylor, K. E., Stouffer, R. J., and Meehl, G. A.: An overview of CMIP5 and the experiment design, Bulletin of the American Meteorological Society, 93, 485, 2012.

Thomason, L. W., Poole, L. R., and Deshler, T.: A global climatology of stratospheric aerosol surface area density deduced from Stratospheric Aerosol and Gas Experiment II measurements: 1984?1994, Journal of Geophysical Research: Atmospheres, 102, 8967–8976, doi:10.1029/96JD02962, http://dx.doi.org/10.1029/96JD02962, 1997.

Tilmes, S., Muller, R., and Salawitch, R.: The Sensitivity of Polar Ozone Depletion to Proposed Geoengineering Schemes, Science, 320, 1201–1204, doi:10.1126/science.1153966, http://science.sciencemag.org/content/320/5880/1201, 2008.

Tilmes, S., Garcia, R. R., Kinnison, D. E., Gettelman, A., and Rasch, P. J.: Impact of geoengineered aerosols on the troposphere and stratosphere, Journal of Geophysical Research: Atmospheres, 114, doi:10.1029/2008JD011420, http://dx.doi.org/10.1029/2008JD011420, d12305, 2009.

Tilmes, S., Richter, J. H., Mills, M. J., Kravitz, B., MacMartin, D. G., Vitt, F., Tribbia, J. J., and Lamarque, J.-F.: Sensitivity of Aerosol Distribution and Climate Response to Stratospheric SO2 Injection Locations, Journal of Geophysical Research: Atmospheres, pp. n/a–n/a, doi:10.1002/2017JD026888, http://dx.doi.org/10.1002/2017JD026888, 2017JD026888, 2017.

Visioni, D., Pitari, G., and Aquila, V.: Sulfate geoengineering: a review of the factors controlling the needed injection of sulfur dioxide, Atmos. Chem. Phys., 17, 3879–3889, doi:10.5194/acp-17-3879-2017, http://www.atmos-chem-phys.net/17/3879/2017/, 2017a.

Visioni, D., Pitari, G., Aquila, V., Tilmes, S., Cionni, I., Di Genova, G., and Mancini, E.: Sulfate geoengineering impact on methane transport and lifetime: results from the Geoengineering Model Intercomparison Project (GeoMIP), Atmospheric Chemistry and Physics, 17, 11 209–

5   11 226, doi:10.5194/acp-17-11209-2017, https://www.atmos-chem-phys.net/17/11209/2017/, 2017b.

Visioni, D., Pitari, G., Tuccella, P., and Curci, G.: Quantification of sulfur deposition changes under sulfate geoengineering conditions, Atmospheric Chemistry and Physics Discussions, 2017, 1–42, doi:10.5194/acp-2017-987, https://www.atmos-chem-phys-discuss.net/acp-2017-987/, 2017c.

Xia, L., Nowack, P. J., Tilmes, S., and Robock, A.: Impacts of Stratospheric Sulfate Geoengineering on Tropospheric Ozone, Atmospheric

10   Chemistry and Physics Discussions, 2017, 1–38, doi:10.5194/acp-2017-434, http://www.atmos-chem-phys-discuss.net/acp-2017-434/, 2017.